Wind-Driven Seasonal Cycle of the Atlantic Meridional Overturning Circulation

JIAN ZHAO AND WILLIAM JOHNS

*Division of Meteorology and Physical Oceanography, Rosenstiel School of Marine and Atmospheric Science,
University of Miami, Miami, Florida*

ABSTRACT

The dynamical processes governing the seasonal cycle of the Atlantic meridional overturning circulation (AMOC) are studied using a variety of models, ranging from a simple forced Rossby wave model to an eddy-resolving ocean general circulation model. The AMOC variability is decomposed into Ekman and geostrophic transport components, which reveal that the seasonality of the AMOC is determined by both components in the extratropics and dominated by the Ekman transport in the tropics. The physics governing the seasonal fluctuations of the AMOC are explored in detail at three latitudes (26.5°N, 6°N, and 34.5°S). While the Ekman transport is directly related to zonal wind stress seasonality, the comparison between different numerical models shows that the geostrophic transport involves a complex oceanic adjustment to the wind forcing. The oceanic adjustment is further evaluated by separating the zonally integrated geostrophic transport into eastern and western boundary currents and interior flows. The results indicate that the seasonal AMOC cycle in the extratropics is controlled mainly by local boundary effects, where either the western or eastern boundary can be dominant at different latitudes, while in the northern tropics it is the interior flow and its lagged compensation by the western boundary current that determine the seasonal AMOC variability.

1. Introduction

The variability of the Atlantic meridional overturning circulation (AMOC) plays a fundamental role in climate change because the AMOC globally redistributes water properties such as heat, freshwater, carbon, and nutrients. Previous studies found that the AMOC varies on time scales from intraseasonal to multidecadal (e.g., Delworth et al. 1993; Hirschi et al. 2007; Biastoch et al. 2008; Köhl and Stammer 2008). These variations have many climatic consequences. For example, the AMOC can drive the Atlantic multidecadal oscillation (AMO) (Knight et al. 2005; Zhang and Wang 2013; Zhang et al. 2014), and a collapse of AMOC will cause widespread temperature decreases over the Northern Hemisphere (Vellinga and Woods 2002). In situ observations also reveal that the mean strength and variability of the northward heat transport at 26.5°N are dominated by the AMOC (Johns et al. 2011).

In the variance spectrum of the AMOC, the seasonal variability has a prominent contribution. Various numerical models with different resolutions and forcings suggest that the fluctuations of the AMOC on time scales shorter than a year are more energetic than at other frequencies, especially south of 40°N (Bingham et al. 2007). Observational data at different latitudes also show that the volume transports associated with AMOC have considerable seasonal changes (Willis 2010; Garzoli and Baringer 2007; Dong et al. 2009). Kanzow et al. (2010) demonstrated that if the seasonal fluctuations are not resolved correctly, the bias induced by the seasonal anomalies might lead to the aliasing of interannual changes or decadal trends inferred from discrete hydrographic observations.

The seasonality of the AMOC used to be seen as primarily generated by the varying Ekman transport and its depth-independent compensation (Bryan 1982; Böning and Herrmann 1994; Jayne and Marotzke 2001). However, recent in situ observations have shown that the geostrophic transport also makes significant contributions to the seasonal AMOC variability. Since April 2004, the strength and vertical structure of AMOC at 26.5°N has been measured by the U.K.–U.S. Rapid Climate Change–Meridional Overturning Circulation and Heatflux Array (RAPID–MOCHA) basinwide full water column array (hereafter the 26.5°N array) (Cunningham

Corresponding author address: William Johns, Division of MPO, Rosenstiel School of Marine and Atmospheric Science, University of Miami, 4600 Rickenbacker Causeway, Miami, FL 33149.
E-mail: bjohns@rsmas.miami.edu

et al. 2007; Kanzow et al. 2007; Rayner et al. 2011). The first 4 yr of the AMOC time series from the 26.5°N array suggested that the seasonal cycle of the AMOC was dominated by the geostrophic midocean and Gulf Stream transports (Kanzow et al. 2010). Other measurements at 41°N and 35°S also confirmed that the geostrophic transport contributes to the seasonal variation of the AMOC (Willis 2010; Garzoli and Baringer 2007; Dong et al. 2009). Therefore, correctly resolving the geostrophic transport is crucial to understanding the seasonal cycle of the AMOC.

The geostrophic transport is largely determined by the zonal density difference between the basin boundaries, so that density anomalies at either boundary will produce fluctuations in the zonally integrated geostrophic transport. For example, at 26.5°N it has been shown that local wind stress curl (WSC) along the eastern boundary is the main factor modifying the density profiles there on seasonal time scales, and the subsequent seasonal cycle of the AMOC (Köhl 2005; Kanzow et al. 2010). However, it remains unknown if similar dynamics occur in other regions such as in the tropical ocean or the South Atlantic. The purpose of this study is to use results from an eddy-resolving numerical model to investigate the seasonal cycle of the AMOC throughout the basin, with a focus on the contribution from the geostrophic transport. In addition, a set of simpler models, including a forced Rossby wave model and a linear two-layer model, are used to help understand the dynamical processes accounting for the seasonal variability.

The paper is organized as follows. The descriptions of numerical models and methods used in this study are presented in section 2. Section 3 describes the simulated AMOC seasonal variations and provides a framework for diagnosing the underlying dynamical mechanisms. Sections 4–6 describe the processes occurring at 26.5°N, 6°N, and 34.5°S in detail, and the dominant mechanisms controlling the AMOC seasonal variation at these latitudes. A discussion and conclusions are given in section 7.

2. Model and methodology

The model used here is an Ocean General Circulation Model for the Earth Simulator (OFES) based on the Modular Ocean Model, version 3 (MOM3). It is configured nearly globally (from 75°S to 75°N) with a horizontal resolution of 0.1°. There are 54 vertical z levels with thicknesses ranging from 5 m at the surface to 330 m for the bottom level (Masumoto et al. 2004). The model is spun up from rest for 50 yr and forced with monthly-mean climatological atmospheric fluxes derived from the 1950–98 National Centers for Environmental Prediction–National Center for Atmospheric Research

(NCEP–NCAR) reanalysis (Kalnay et al. 1996). After that, the model is driven by daily-mean NCEP–NCAR reanalysis data from 1950 to 2009 (Sasaki et al. 2008; Masumoto 2010). In the present study, the output over 1980–2009 is averaged to derive a climatological seasonal cycle.

To help interpret the dynamics involved in the seasonal AMOC cycle, a two-layer model with realistic topography is also used. The model is linearized with the following governing equations:

$$\frac{\partial u_i}{\partial t} - f v_i = -P(x) + A \nabla^2 u_i + F(x) - \lambda \frac{u_i}{H_i},$$

$$\frac{\partial v_i}{\partial t} + f u_i = -P(y) + A \nabla^2 v_i + F(y) - \lambda \frac{v_i}{H_i}, \quad \text{and}$$

$$\frac{\partial H_i}{\partial t} = \frac{\partial u_i H_i}{\partial x} + \frac{\partial v_i H_i}{\partial y},$$

where $i = 1$ (upper layer) or 2 (lower layer), u and v are zonal and meridional velocity, f is the Coriolis parameter, $A = 1.2 \times 10^3 \, \mathrm{m^2 \, s^{-1}}$ is a lateral viscosity coefficient, $\lambda = -5 \times 10^{-5}$ is a bottom friction coefficient, and H is layer thickness. The bottom friction is usually applied only in the bottom layer, but also acts in the top layer when $H_2 = 0$. The pressure gradient term P is

$$P(k) = \begin{cases} g \dfrac{\partial h_1}{\partial k} & \text{for layer 1} \\[2ex] g \dfrac{\partial h_1}{\partial k} + g' \dfrac{\partial h_2}{\partial k} & \text{for layer 2} \end{cases}, \quad \text{where}$$

$$k = x \quad \text{or} \quad y,$$

g is gravitational acceleration, $g' = g(\rho_2 - \rho_1)/\rho_2$, ρ_i is layer density ($i = 1$ or 2), h_1 is the sea surface height, and h_2 is the interface anomaly.

The forcing term is concentrated in the upper layer:

$$F(k) = \begin{cases} \tau_k & \text{for layer 1} \\ 0 & \text{for layer 2} \end{cases},$$

where $k = x$ or y. The wind stress forcing is the climatological monthly field derived from the wind stress used in OFES between 1980 and 2009. The initial upper-layer thickness is 1000 m, and the density difference between the upper and lower layers is 1 kg m^{-3}.

The model domain covers the region from 56°S to 55°N and 100°W to 25°E with a uniform spatial resolution of 0.25°. Buffer zones are implemented at the southern and northern boundaries and along the eastern boundary south of 35°S to damp artificial boundary waves. Bottom

topography comes from the 5-Minute Gridded Global Relief Data (ETOPO5) bathymetry dataset interpolated onto the model grid, and the minimum water depth is 200 m. The same winds that force the OFES (NCEP–NCAR reanalysis) are used to force the two-layer model. The two-layer model is integrated for 25 yr, and the results from the last 5 yr are used to derive a climatological annual cycle. There is no thermohaline forcing in the two-layer model, and therefore its time-varying AMOC is driven only by winds; it is also missing the large-scale thermohaline circulation present in the OFES.

In addition, daily measurements of AMOC from the 26.5°N array between April 2004 and April 2011 are used to evaluate the numerical results. Following the AMOC decomposition of the observational data (Rayner et al. 2011), the northward upper-ocean flow of the AMOC is decomposed into its three main components: the Gulf Stream transport through the Straits of Florida (GS), the Ekman transport in the top 100 m (EK), and the upper-midocean transport between the Bahamas and Africa (UMO). Further details about the estimation of each component may be found in Rayner et al. (2011).

In both OFES and the in situ data, the AMOC strength at a certain latitude is defined as the maximum of the vertical streamfunction: $\Psi(z, y, t) = \int_{x_w}^{x_e} \int_z^0 v(x, y, z, t) \, dz \, dx$, where x_w and x_e are the western and eastern boundaries, and $v(x, y, z, t)$ is the meridional velocity. The AMOC in the two-layer model is calculated from the upper-layer meridional velocity. Similar to that derived from hydrographic sections (Talley et al. 2003; Lumpkin and Speer 2007), the mean structure of the meridional streamfunction in OFES (Fig. 1) is
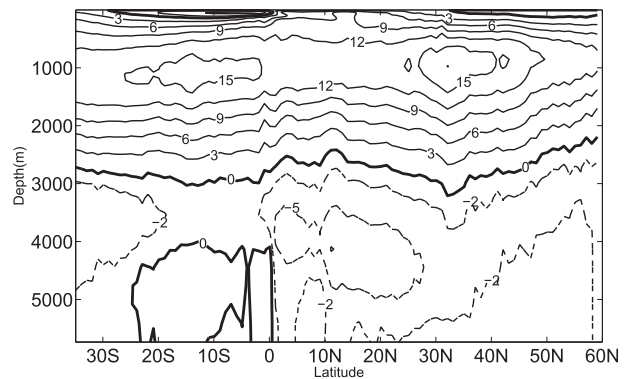

FIG. 1. The mean structure of the AMOC simulated in OFES (1980–2009) (Sv).

composed of two meridional overturning cells located between the surface and about 3000 m and from 3000 m to the bottom, respectively. The 1980–2009 average AMOC strength has a maximum of 18 Sv at 35°N. At 26.5°N, the mean AMOC is 16 Sv, which is slightly weaker than the measured 7-yr mean value of 17.4 Sv from the 26.5°N array (April 2004–April 2011). This study is mainly focused on the upper cell that involves the northward flow within approximately the top 1100 m and the compensating southward flow from 1100 to 3000 m.

3. Seasonal cycle of the AMOC

a. Seasonal variability in OFES

The AMOC estimated from the OFES between 1980 and 2009 is used to derive a climatological annual cycle. Figure 2 shows the distribution of the AMOC anomaly with respect to latitude and month. The most significant
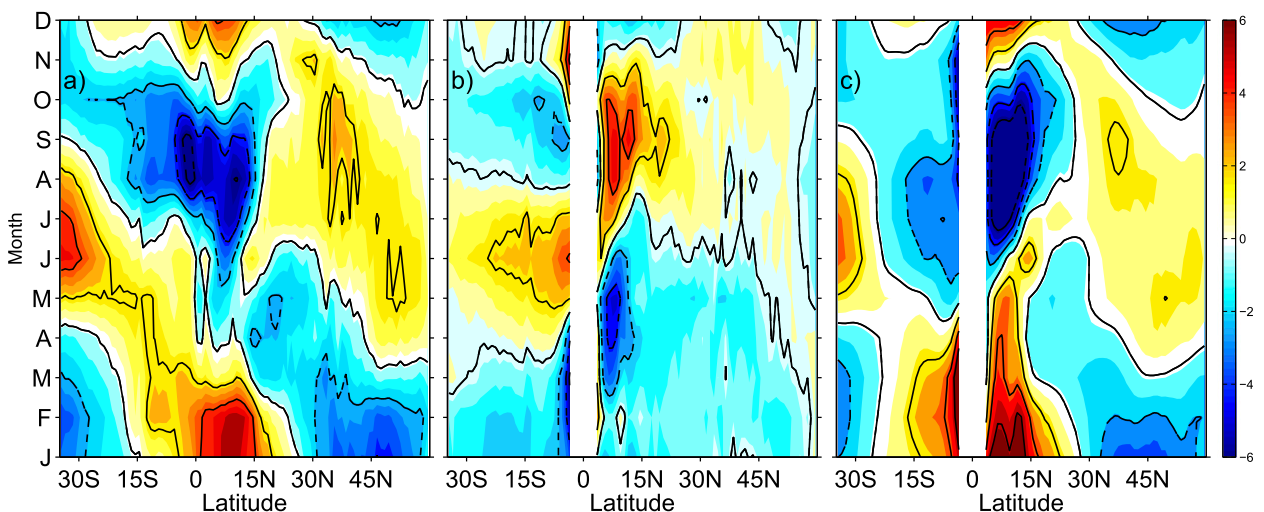

FIG. 2. The seasonal anomaly field derived from the monthly OFES result (1980–2009) for (a) AMOC, and the (b) geostrophic and (c) Ekman components. Contour interval is 2 Sv. The 3°S–3°N equatorial band is excluded from (b) and (c).

seasonal variability takes place in the tropical Atlantic region with 11-Sverdrup (Sv; $1\,\mathrm{Sv} \equiv 10^6\,\mathrm{m}^3\,\mathrm{s}^{-1}$) peak-to-peak amplitude and a maximum (minimum) in boreal winter (fall). Outside of the tropics, the amplitudes are much weaker (4–6 Sv), and the phases are also different from that in the tropical ocean. While the Northern Hemisphere subtropics have a broad maximum in boreal summer and fall and minimum in winter and spring, the southern subtropical ocean reaches its maximum in austral winter and minimum in austral fall. In most latitudes, the phases are generally coherent within about 10°–15°, meaning that the seasonal cycle along one latitude is representative for about a 10°–15° meridional extent. The amplitudes of the seasonal variability are significant in comparison to the AMOC variability on interannual time scales in the model, which have rms values ranging from 0.5 to 1.5 Sv at different latitudes.

On seasonal time scales, the meridional flow can be split into Ekman and geostrophic components provided that the non-Ekman ageostrophic flow is negligible. This assumption is confirmed by Baehr et al. (2004) and Hirschi and Marotzke (2007), who demonstrated that the thermal wind and the Ekman contributions are the dominant terms in the force balance governing the meridional flow, with generally smaller contributions from other terms.

The Ekman contribution is calculated from zonal wind stress:

$$\Psi_{\mathrm{ek}}(y,t) = \int_{x_w}^{x_e} \frac{-1}{\rho f}\,\tau_x(x,y,t)\,dx,$$

where τ_x, ρ, f, x_w, and x_e are the zonal wind stress, reference density, Coriolis parameter, and western and eastern boundaries, respectively. The geostrophic contribution to the AMOC is estimated by removal of the Ekman transport from the total meridional transport above h_{moc}, where h_{moc} is the depth where the maximum Ψ occurs.

As shown in Fig. 2, both the Ekman and geostrophic anomalies have substantial changes throughout the year, indicating that both contribute to the seasonal cycle of the AMOC. Similar to the AMOC, their peak-to-peak amplitudes are largest in the tropical ocean and decrease toward higher latitudes. In the tropics, the Ekman anomaly is characterized by positive values for the first half of the year and negative values in the second half of the year. The corresponding geostrophic variability is nearly out of phase with the Ekman contribution in the northern tropics but has a more complicated relationship in the southern tropics. In the subtropics, the phase of the geostrophic component shifts by 2–3 months relative to the tropics and shows an asymmetry between the Southern and Northern Hemispheres.

The amplitude of the Ekman transport anomalies is generally larger than the geostrophic transport, but because of the varying phase relationships between them, the total AMOC variability at any latitude can be either enhanced or diminished relative to the individual components. For example, in the tropics near 8°N, the amplitudes of Ekman and geostrophic anomalies are 15 and 8.5 Sv, respectively, but the AMOC only has an 11-Sv peak-to-peak fluctuation. On the other hand, AMOC has stronger variability than either the Ekman or the geostrophic transport in subtropical regions, indicating less compensation between them.

b. Comparison to observations at 26.5°N

To examine if the OFES results are consistent with observations, the climatological seasonal variability of the AMOC from the monthly-mean OFES time series and the 26.5°N array is compared. The seasonal cycle of the observed MOC (Fig. 3a) exhibits a 6-Sv peak-to-peak amplitude with a maximum northward flow in July and October and a minimum in March. A similar phase occurs in OFES (Fig. 4a) but with a smaller amplitude (4 Sv). While the seasonal cycle of OFES shown in Fig. 4 is derived from 30 yr of data (1980–2009), the seasonal cycle derived from the same time period as the in situ observations (2004–09) gives essentially the same result.

The breakdown of the AMOC seasonal cycle at 26.5°N into its three main components (GS, EK, and UMO) for both the observations and OFES is also shown in Figs. 3 and 4. The GS refers to the transport carried by the Florida Current. The mean strength of the observed GS is 31.5 Sv, and its seasonal cycle (Fig. 3b) shows an annual range of 4 Sv with peak in July and minimum in November. Note that the seasonal cycle of the GS shown here is slightly stronger than that in Kanzow et al. (2010) because of the longer period used in our study. Nevertheless, both the amplitude and phase displayed here are consistent with the seasonal cycle computed from the 26-yr-long time series of the Florida Current (Kanzow et al. 2010). The Ekman transport varies from 1.2 Sv in February to 4.6 Sv in July, which is slightly different from Kanzow et al. (2010). This is mainly due to the longer time period included in our estimate of the seasonal cycle at 26.5°N [2004–11 vs 2004–08 in Kanzow et al. (2010)] and to the substantial zonal wind stress anomalies that occurred between December 2009 and March 2010 associated with a strong negative phase of the North Atlantic Oscillation (NAO) (McCarthy et al. 2012). The seasonal change of UMO is about 5 Sv, from −18.9 Sv in March to −13.8 Sv in October. The sum of the peak-to-peak variations of the three separate components is 12.5 Sv, much larger than
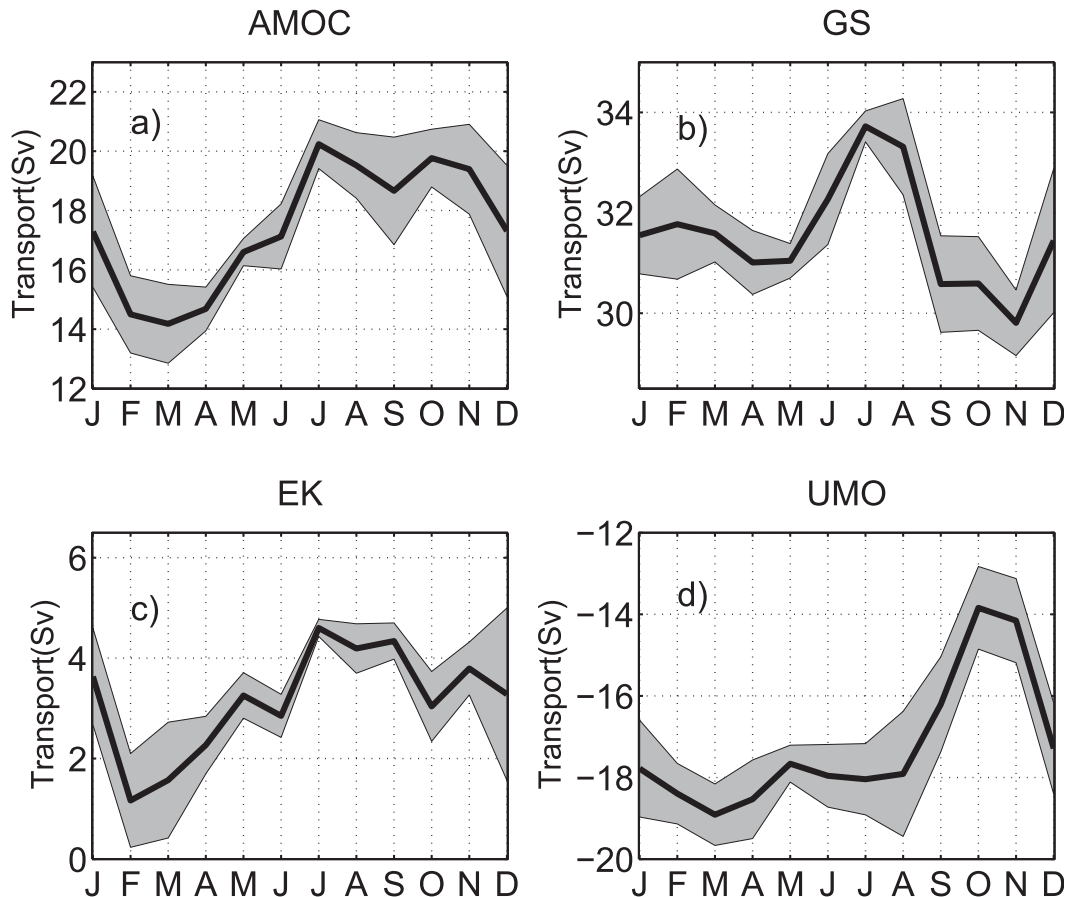
FIG. 3. Seasonal cycle (black solid lines) of (a) AMOC, (b) GS, (c) EK, and (d) UMO, as obtained from monthly averages of the 26.5°N time series between April 2004 and April 2011. The gray envelopes represent the std error of each month.

that of the AMOC (6 Sv), indicating that compensation occurs among the three individual components.

The same decomposition applied to the OFES (Fig. 4) shows that while the GS in OFES has an annual cycle similar to the observations, both the peak-to-peak amplitude (1.3 Sv) and the mean strength (22.3 Sv) are much smaller. Like the GS, the seasonal cycle of UMO in OFES displays a similar phase with that in the observations, but with a weaker amplitude (2.5 Sv) and weaker annual-mean value (−10 Sv). The reason for this discrepancy is that, in OFES, part of the western boundary current (WBC) does not flow through the Straits of Florida; instead it is located east of the Bahamas, where it is included here in the UMO transport. In the OFES, the northward transport in this "Antilles" Current is about 14 Sv in the top 1100 m. In the real ocean, the majority of the western boundary flow is through the Straits of Florida, and only a 6 Sv northward Antilles Current occurs east of Abaco, Bahamas (Lee et al. 1996; Johns et al. 2008). The total northward western boundary flow in OFES is about 36 Sv and nearly

equal to the sum of the observed Florida Current (31.5 Sv) and Antilles Current (6 Sv) transports. The weaker UMO seasonal amplitudes in OFES compared to the observations is attributed to the too weak wind stress curl near the eastern boundary in the OFES model, and a detailed explanation is given in the following section. The phase and amplitude of the Ekman transport in OFES generally agrees with the observed annual cycle, that is, a peak in July and minimum in March. Their differences can be attributed to the different wind products used [NCEP–NCAR reanalysis for OFES and cross-calibrated multi-platform (CCMP) winds for the 26.5°N array] and in part to the different time period used in OFES (1908–2004) and the 26.5°N array (2004–11).

c. Dynamics of the seasonal cycle

In the following, we will investigate the main physical process governing the AMOC seasonal cycle at different latitudes. It is well known that the meridional Ekman transport is directly driven by the zonal wind that is closely linked to changes in atmospheric circulation. For
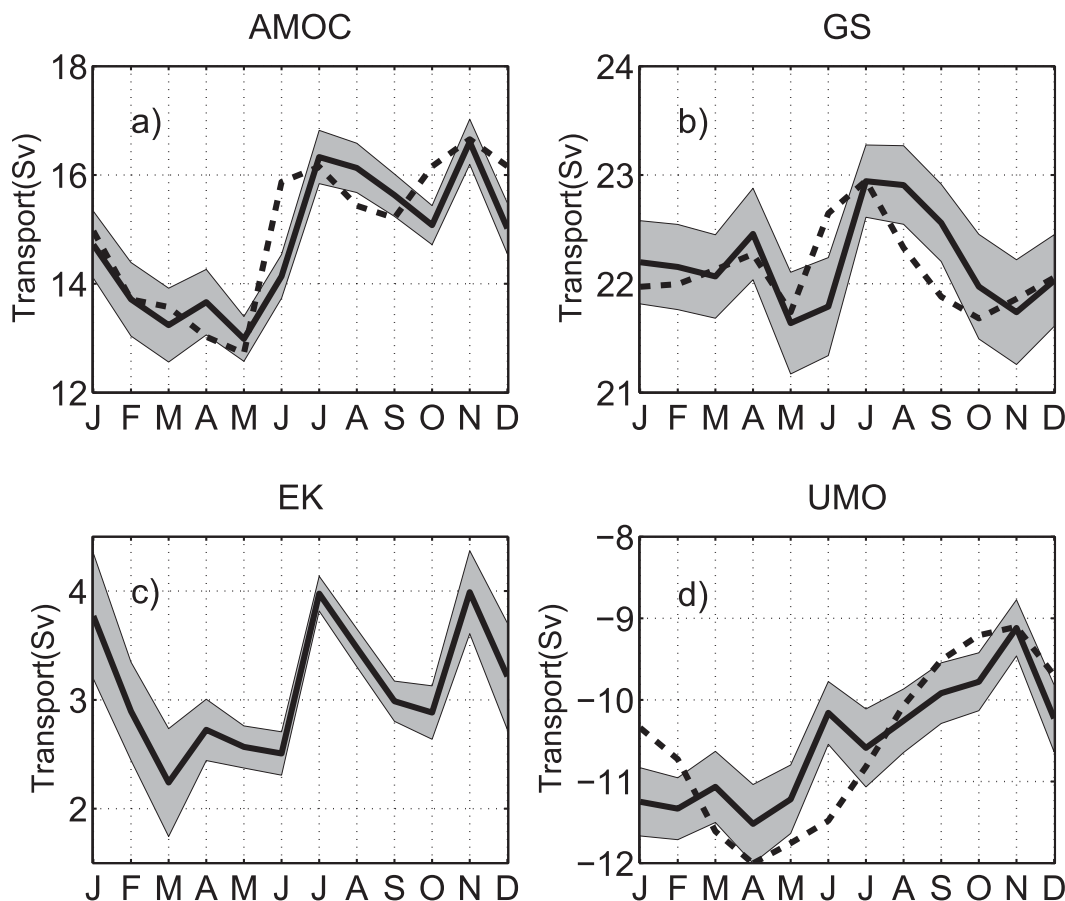
FIG. 4. As in Fig. 3, but for the climatological annual cycle derived from the OFES (1980–2009). Dashed lines are calculated from the two-layer model simulation, where the annual mean from OFES is added to the two-layer result. (The Ekman contribution is the same for both models.)

instance, the seasonal fluctuations of the tropical Ekman transport are mainly associated with the annual migration of the intertropical convergence zone (ITCZ). These changes in Ekman transport affect the AMOC directly and immediately through changes in the meridional surface layer transport. On the other hand, the variations of the geostrophic transport involve both barotropic and baroclinic adjustment. The barotropic flow adjusts rapidly to changes in atmospheric forcing and approaches a quasi-equilibrium "topographic Sverdrup" balance after transients such as the barotropic basin modes die out (Anderson et al. 1979). The structure of this barotropic response depends crucially on the actual basin topography. On the other hand, the baroclinic flow involves both the dynamics in a flat bottom ocean and the influences of topography. Locally, the baroclinic geostrophic velocity can be estimated with density profile pairs and a level of "no motion." The basinwide profile of the baroclinic geostrophic transport is determined by the density difference between the end points of the basin (Baehr et al. 2004). Consequently,

variations in the AMOC associated with baroclinic flow changes are closely linked to the changes of the density profiles at the basin boundaries.

WBCs provide a good example of how topography affects both barotropic and baroclinic adjustment. WBCs are usually located, at least partly, in relatively shallow regions, such as GS. Their mean strength is determined to the first order by the Sverdrup balance established by baroclinic planetary waves, which is not strongly affected by topography (Anderson and Gill 1975; Anderson and Killworth 1977). However, WBC fluctuations on periods much shorter than the time taken for baroclinic adjustment (several years) are largely disconnected from the baroclinic planetary waves. For instance, the seasonal variability of the GS at 26.5°N is largely controlled by the forcing north of the Straits of Florida through boundary wave processes (Anderson and Corry 1985; Atkinson et al. 2010; Czeschel et al. 2012).

To investigate the above dynamics in a simple context, a linear two-layer model with realistic topography is configured to simulate the seasonal cycle of the AMOC.
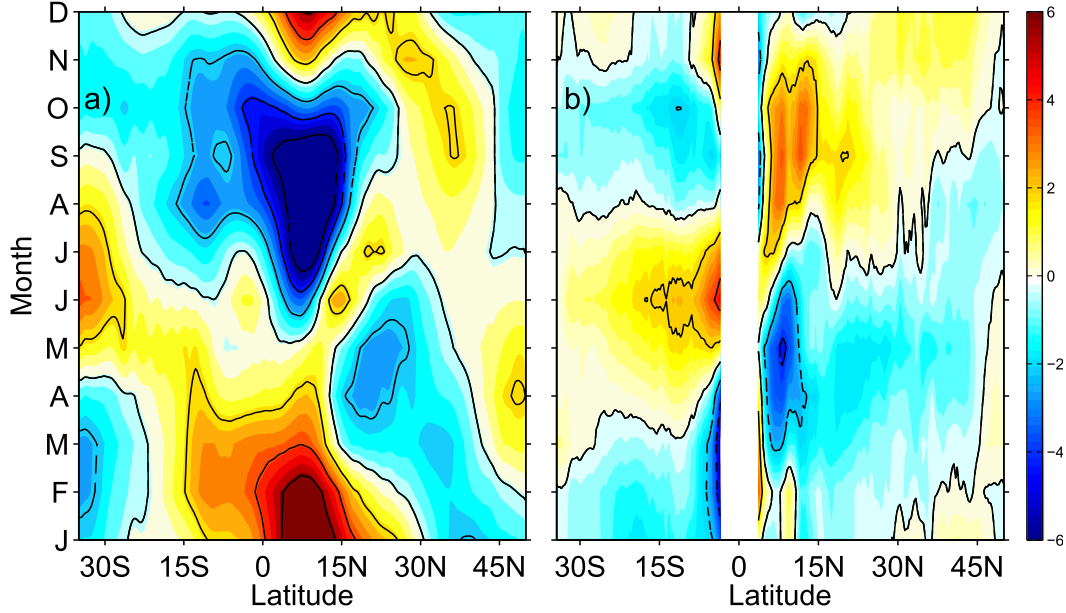
FIG. 5. Seasonal cycle of (a) AMOC and (b) geostrophic transport from two-layer model (Sv).

The two-layer model, described in section 2, includes both barotropic and baroclinic adjustment induced by wind forcing. As illustrated in Fig. 5, the seasonal cycle of AMOC and geostrophic transport in the two-layer model generally agrees with those of OFES (cf. Fig. 2). In particular, the phases and amplitudes of the seasonal cycle in both the tropics and subtropics are well reproduced. The main difference between the two-layer model and OFES is at higher latitudes in the North Atlantic, where the seasonal variability is underestimated. This is probably the result of the damping applied along the northern boundary to prevent artificial boundary wave propagation effects, but could also be due to nonlinear processes associated with the Gulf Stream in OFES. Nevertheless, the similarity in both phases and amplitudes in OFES and the two-layer model demonstrates that the linear two-layer model successfully captures the fundamental features of the seasonal AMOC variation.

d. Roles of barotropic and baroclinic processes

To better understand the dynamics contained in both OFES and the two-layer model, we explore the roles of barotropic and baroclinic processes in modulating the seasonal variability of the AMOC. Because the same wind forcing is used in both models, their Ekman transports are exactly the same, and we will focus on the comparison of meridional geostrophic transport in both models. To perform a comparative analysis between the two models, we define an "upper-layer" and "lower-layer" geostrophic velocity in OFES as the respective vertically averaged flows above and below the depth of the maximum of the AMOC streamfunction h_{moc} at any given time:

$$v_1(x,y,t) = \frac{1}{h_{moc}} \int_{h_{moc}}^{0} [v(x,y,z,t) - v_{ek}(x,y,z,t)] \, dz \quad \text{and}$$

$$v_2(x,y,t) = \frac{1}{D - h_{moc}} \int_{H}^{h_{moc}} v(x,y,z,t) \, dz,$$

where D is the local water depth, v is the full velocity, and v_{ek} is the Ekman velocity.

We further define a "baroclinic" velocity for the upper-layer flow as $v' = v_1 - v_2$. Thus, in OFES, for any region with bottom depths shallower than h_{moc}, $v_2 = 0$ and $v' = v_1$. For the two-layer model, v_1 and v_2 are simply equal to the upper- and lower-layer velocity and v' is defined as above.

In what follows, we will use the upper-layer geostrophic streamfunction accumulated from the eastern boundary,

$$\Psi_1(x,t) = \int_{x}^{x_e} \int_{h_{moc}}^{0} v_1(x,t) \, dz \, dx = h_{moc} \int_{x}^{x_e} v_1(x,t) \, dx,$$

as a primary tool in evaluating the AMOC variability. According to the above definitions, we can also break this down into a baroclinic component,

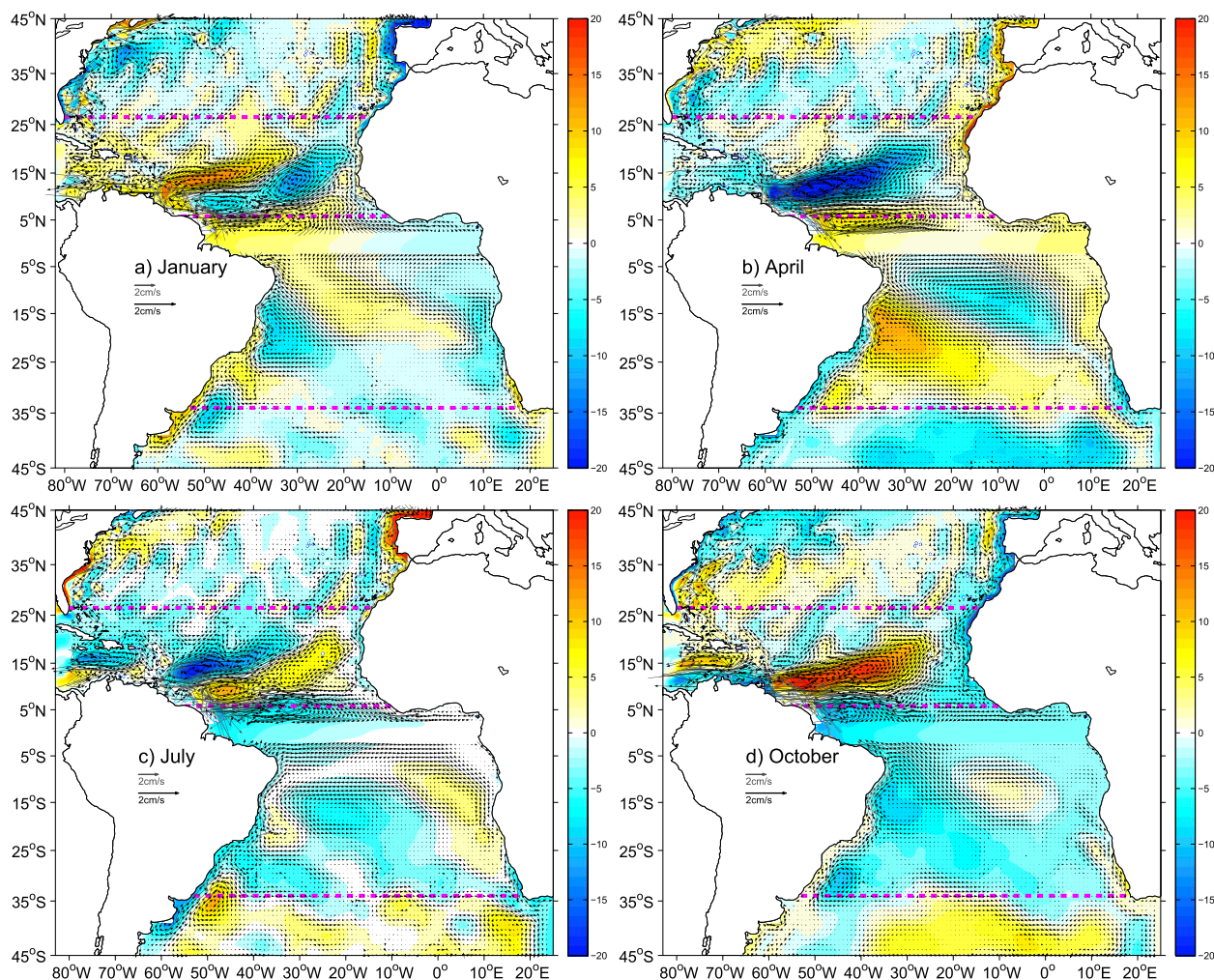$$\Psi_{bc}(x,t) = \int_{x}^{x_e} \int_{h_{moc}}^{0} v'(x,t) \, dz \, dx = h_{moc} \int_{x}^{x_e} v'(x,t) \, dx,$$

FIG. 6. Interface anomaly (color shading; m) and upper-layer baroclinic velocity v' (cm s^{-1}) in the two-layer model for (a) January, (b) April, (c) July, and (d) October. For better visualization, the stronger currents (gray) and weaker currents (black) are shown in different scales. Dashed magenta lines indicate the three latitudes where the AMOC is diagnosed: 26.5°N, 6°N, and 34.5°S.

and a barotropic component,

$$\Psi_{bt}(x,t) = \int_x^{x_e} \int_{h_{moc}}^0 v_2(x,t)\,dz\,dx = h_{moc} \int_x^{x_e} v_2(x,t)\,dx,$$

where the latter represents the part of the upper-layer meridional flow that is common to both layers.

As a further aid in interpreting the results, we show in Fig. 6 the monthly anomalies of the upper-layer baroclinic velocity v' and the associated interface anomaly h_2 from the two-layer model for January, April, July, and October. In the following sections, we select three representative latitudes to diagnose the AMOC variability in detail: two in the Northern and Southern Hemisphere extratropics (26.5°N and 34.5°S) and one in the northern tropics (6°N), which are denoted in Fig. 6a.

4. AMOC seasonal cycle at 26.5°N

a. Seasonal variability of the upper-layer streamfunction

Figures 7a and 8a show the seasonal anomalies of the upper-layer cumulative streamfunction Ψ_1 at 26.5°N in OFES and the two-layer model, respectively. Both models show a similar basinwide pattern with predominantly negative anomalies in the first half of the year (January–June) and positive anomalies in the second half of the year (July–November). Interspersed within these broad zonal patterns are local maxima and minima that are tilted westward (which is more clearly evident in the OFES model), indicating westward propagation. The OFES model pattern is generally noisier than the two-layer model, which can be attributed to the
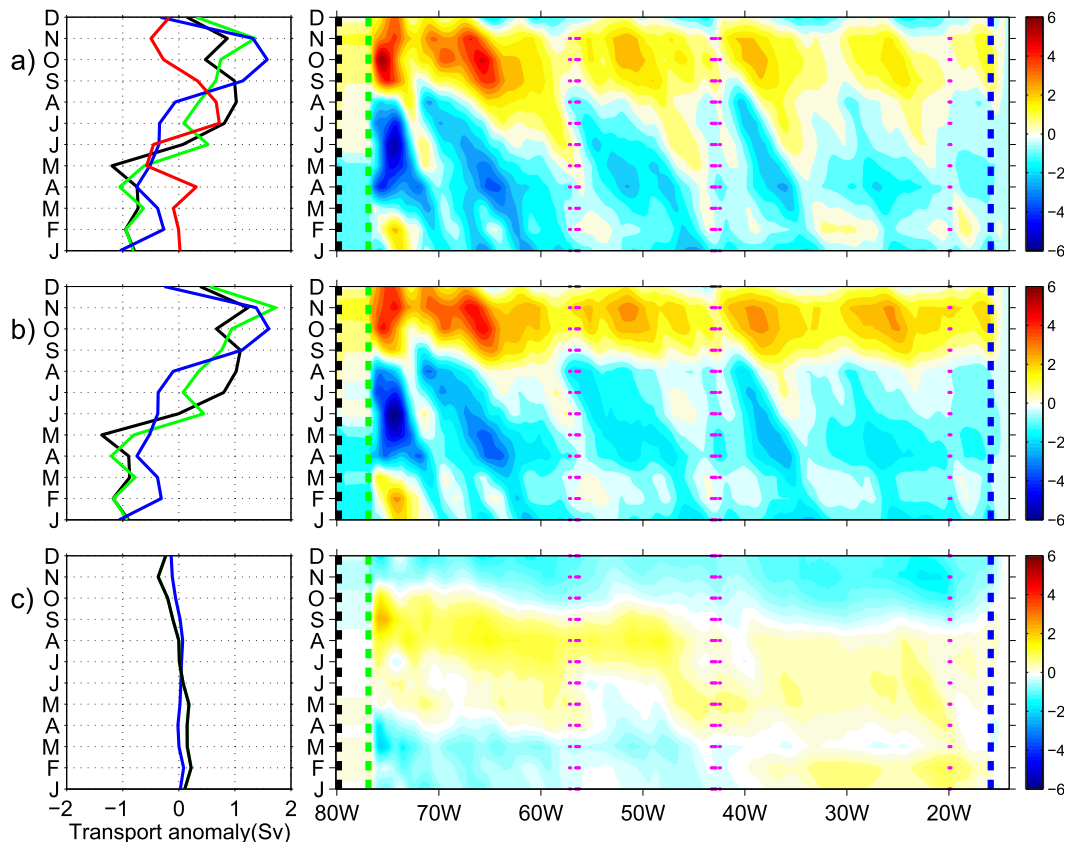
FIG. 7. Seasonal cycle of the (a) upper-layer meridional geostrophic streamfunction (Ψ_1), (b) baroclinic streamfunction (Ψ_{bc}), and (c) barotropic streamfunction (Ψ_{bt}) at 26.5°N in OFES(1980–2009). See text for the definitions of barotropic and baroclinic streamfunction. The dashed lines mark the locations for the offshore edge of the eastern boundary layer (blue), western boundary point of the interior ocean (green), and the western basin boundary (black). The seasonal cycle at the three points in each streamfunction are shown at the left in their corresponding colors. Red line denotes the GS. The significance of the seasonal cycle at each longitude is determined by checking if the peak-to-peak amplitude is larger than the std error. The std error for each month is estimated by dividing its interannual variations by the number of degrees of freedom (DOFs). The insignificant regions are marked by magenta dots (Sv).

fact that it is interannually forced, rather than forced by a repeating seasonal cycle as in the two-layer model, and also because it is an eddy-resolving model and therefore contains random mesoscale features that can leave a residual imprint on the climatological annual cycle. Otherwise, the two patterns are quite similar.

Before discussing these results further, we refer the reader to Fig. 9, which helps to better explain the nature of these seasonal Ψ_1 patterns. Figure 9a shows the time series of local upper-layer transport [i.e., $v_1(x, t)$ multiplied by h_{moc} and dx] from the last 5 yr of the two-layer model simulation at 26.5°N, while Fig. 9b shows the associated pattern for the cumulative streamfunction Ψ_1. Near the eastern boundary, the local meridional transport has a strong seasonal variation with a minimum in April and maximum in October (Fig. 9a). This variability is forced by a strong annual cycle of wind stress curl at the eastern boundary through the same mechanism

described previously by Kanzow et al. (2010), that is, by seasonal uplift and depression of the thermocline near the coast that drives a seasonally varying eastern boundary flow. Emanating from the western edge of this boundary zone are meridional velocity anomalies (Fig. 9a) associated with annual baroclinic Rossby waves that propagate westward at a first baroclinic mode wave speed (the only baroclinic mode supported by the two-layer model). At 26.5°N, these waves interact with the Canary Islands just west of the eastern boundary, which locally disturbs the westward phase propagation between about 17° and 19°W. This is a very localized effect that is not present at neighboring latitudes, where the Rossby wave crests and troughs propagate smoothly away from the eastern boundary, and it has no consequential effect on the basinwide transport.

As the Rossby waves propagate across the ocean interior, their signal is affected by the local wind stress curl
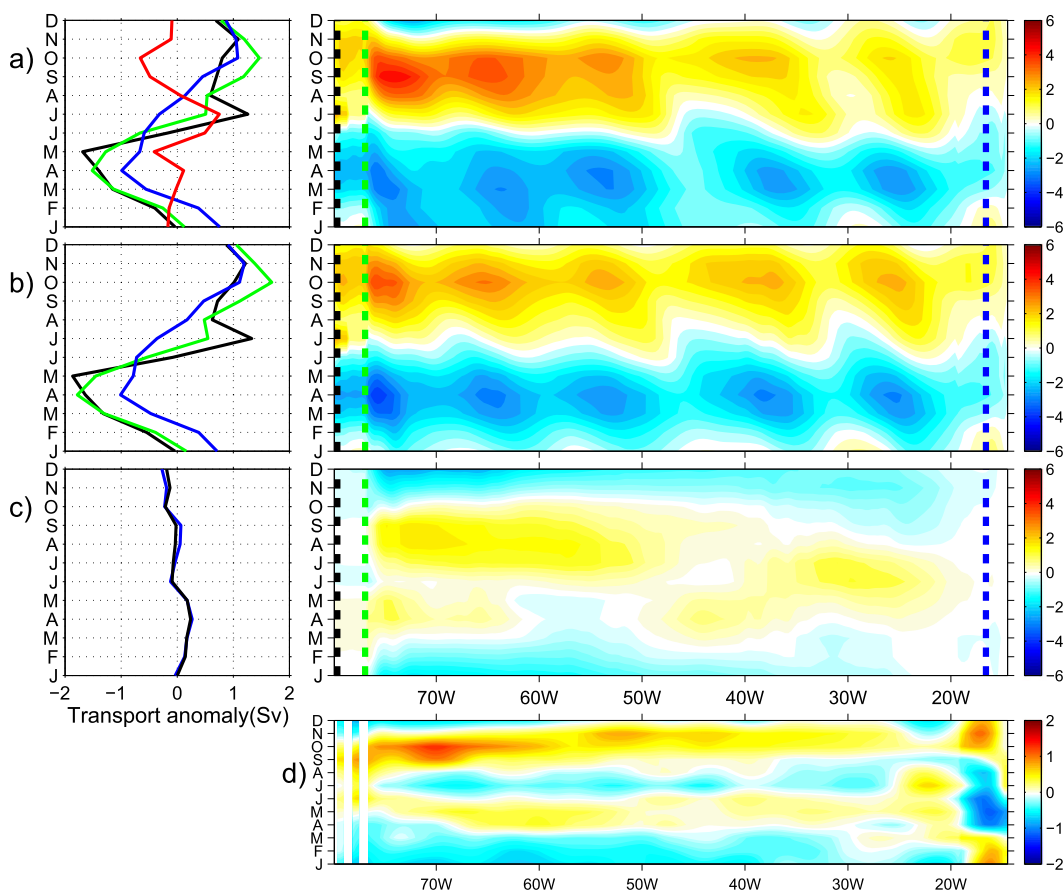
FIG. 8. (a)–(c) As in Fig. 7, but for the two-layer model at 26.5°N. The two-layer model has an exactly repeating annual cycle so there is no error for each month. (d) Wind stress curl calculated from the wind forcing used in the two-layer model along 26.5°N ($10^{-7}\,\mathrm{N\,m^{-3}}$).

forcing along the wave paths and interactions with topography, so that their amplitude is modified, and also they are weakly damped by both lateral and bottom friction. The cumulative streamfunction shown in Fig. 9b reflects, in the east, the initial contribution from the annually reversing eastern boundary flow, and then it is modulated toward the west by zonal integration across the crests and troughs of the propagating Rossby wave pattern.

As the waves approach the Bahamas (77°W), their meridional velocity signal is amplified by interaction with the Bahamas boundary, which leads to increased amplitudes near 75°W and steadily decreasing amplitudes from there to the Bahamas, with a nearly stationary phase across this boundary region (Fig. 9a). This behavior is consistent with expectations from linear Rossby wave reflection at the western boundary, due to the superposition of the long waves and reflected short Rossby waves (Longuet-Higgins 1964; Pedlosky 1987). Local wind stress curl forcing near the Bahamas can also contribute to the meridional transport anomalies here,

but this effect is relatively weak compared to the wave reflection/interaction process. The net effect of this wave reflection process is to strongly reduce the amplitude of the pressure anomaly and hence the cumulative streamfunction anomaly (Ψ_1) at the Bahamas boundary, due to the compensation of the zonally integrated flow across the rest of the basin by an opposing meridional flow near the boundary. This has been clearly demonstrated in observations, as well as in a theoretical/modeling context, by Kanzow et al. (2009). The cumulative streamfunction anomaly at the Bahamas boundary is typically reduced by about a factor of 3 relative to its seasonal amplitude a few degrees into the interior. As shown by Kanzow et al. (2009), local boundary waves are involved in this process as well as short Rossby waves, and therefore it should be described in general as a western boundary wave reflection/interaction process.

A further, but relatively small, modification of the cumulative streamfunction occurs cross the Straits of Florida due to the seasonal cycle of the GS transport, leading to the total AMOC seasonal cycle shown at the
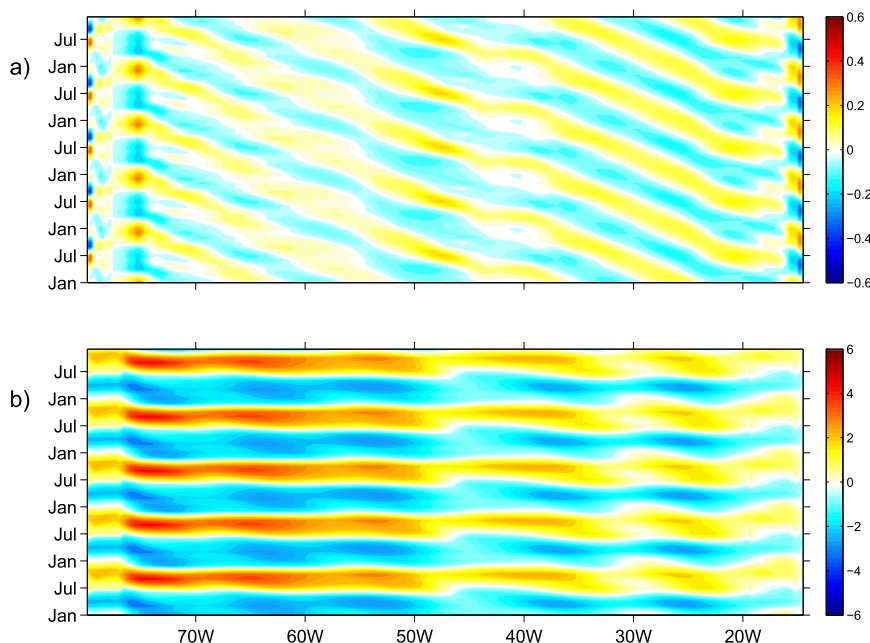
FIG. 9. Upper-layer (a) local meridional transport and (b) cumulative streamfunction for the last 5 yr of the two-layer model simulation at 26.5°N. The local meridional transport is calculated from the meridional geostrophic velocity weighted by h_{moc} and grid distance dx. The upper-layer streamfunction is the zonal accumulation of the local meridional transport from the eastern boundary (Sv).

western boundary in Fig. 9b. (Note that the pattern of Ψ_1 shown in Fig. 8a is exactly the same as that of any of the individual years of Fig. 9b.) The local meridional transport and Ψ_1 over multiple years in OFES (not shown) has a similar structure to that shown in Fig. 9, but is more variable due to the interannual forcing.

Returning to Figs. 7 and 8, we show in the left of these figures the role of different regions in determining the seasonal variability of the zonally integrated meridional geostrophic transport. These curves show the seasonal cycle near the eastern basin boundary, western point of the interior ocean, and western basin boundary. A point twice the Rossby deformation radius away from the eastern basin boundary is selected as the eastern point, while the Bahamas Islands are chosen as the western point of the interior ocean. From the eastern boundary to about 17°W, the geostrophic transport sets up a seasonal cycle with a maximum in September–November and minimum in March–May. This feature is consistent in both numerical models (blue line in Figs. 7 and 8) and is forced by the wind stress curl near the eastern boundary (Fig. 8d). West of 17°W, the seasonal variability is modified until it reaches a relatively stable amplitude near 77°W. The fluctuations of the amplitudes have a spatial scale about 15° in longitude for both models. As noted above, this westward-propagating pattern is induced by the meridional velocity associated

with westward-propagating long Rossby waves (Fig. 9). Although the wavelike structure leads to substantial changes of the local meridional transport in the interior, when integrated across the full width of the basin, including the effects of wave reflection at the western boundary, the cumulative streamfunction anomaly at the western edge of the interior ocean (the Bahamas) is not greatly changed from that at the offshore edge of the eastern boundary layer. West of 77°W, the zonally integrated transport is further modified due to the impact of the Gulf Stream. The differences between the green and black lines in Figs. 7a and 8a indicate the seasonal cycle of the Gulf Stream (red line).

It is worthwhile to note that while the exact phase of the wave structures across the interior (and the number of maxima and minima in the cumulative streamfunction) depends on the first-mode baroclinic wave speed, the zonally integrated streamfunction anomaly at the western edge of the interior (the Bahamas) is largely insensitive to this. We have tested this in the two-layer model using different choices of the stratification parameter (g'), which controls the first-mode wave speed, and find no significant differences in the cumulative streamfunction anomaly at the Bahamas when varying this wave speed over a factor of 3. This is again because of the strong compensating effect produced by the wave reflection process: this largely nullifies the meridional
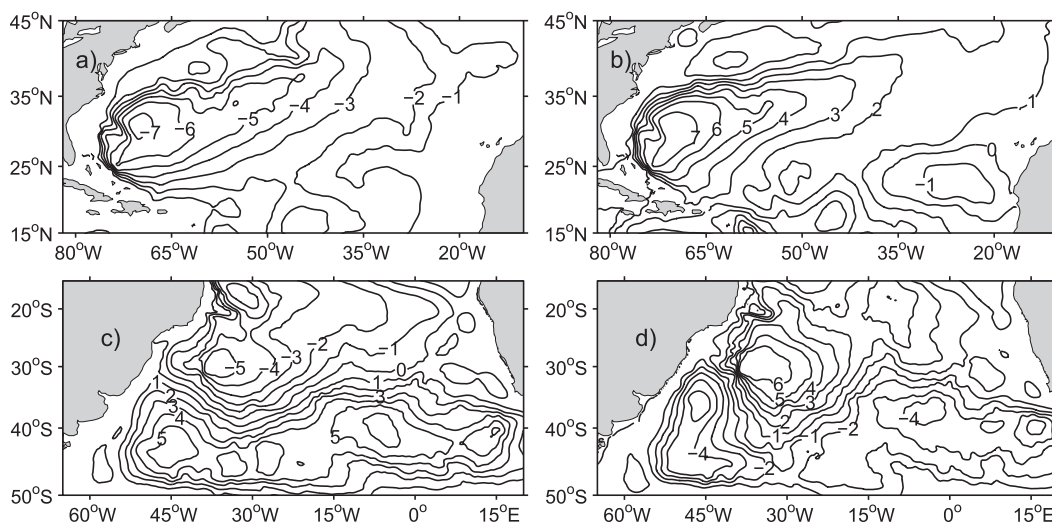
FIG. 10. The barotropic streamfunction anomaly calculated from the two-layer model for the North Atlantic in (a) February and (b) September and for the South Atlantic in (c) February and (d) June (Sv). The barotropic streamfunction is calculated from the meridional velocity from surface to bottom.

transport anomaly associated with the waves impinging on the Bahamas, irrespective of the exact phase of the impinging wave.

b. Barotropic and baroclinic contributions to the upper-layer streamfunction

In Figs. 7 and 8, we show in addition to Ψ_1 the contributions of the barotropic (Ψ_{bt}) and baroclinic (Ψ_{bc}) components of the upper-layer streamfunction in both models. In contrast to the upper meridional geostrophic transport (Ψ_1), Ψ_{bt} has weaker seasonal variations of approximately ± 2-Sv amplitude across the interior, and Ψ_{bt} makes a negligible contribution to Ψ_1 when integrated across the full basin. The phase of the Ψ_{bt} anomalies across the interior is different from Ψ_1 and shows maximum positive values in fall and negative values in winter. Unlike the Rossby wave anomalies that dominate the interior pattern of Ψ_1, Ψ_{bt} is associated with the seasonal spinup and spindown of a large-scale barotropic gyre in the North Atlantic that is driven by the large-scale seasonal wind stress curl forcing. As shown in Figs. 10a and 10b, the barotropic gyre is largely closed over the deep part of ocean and does not extend up onto the continental shelves, so that there is no significant seasonal variability at the eastern boundary nor at the western interior point or at the western boundary (Figs. 7c and 8c). As a result, the barotropic adjustment does not contribute to the seasonal cycle of the meridional geostrophic transport at 26.5°N.

The overall pattern of Ψ_1 is very similar to Ψ_{bc}, indicating that the oscillations in Figs. 7a and 8a are produced mainly by baroclinic processes. Near the eastern

boundary, the minimum and maximum of the Ψ_{bc} (blue line, Figs. 7b and 8b) are consistent with the uplift and depression of the thermocline along the eastern boundary (Figs. 6b,d). The interior thermocline anomalies shown in Fig. 6 are associated with the westward-propagating Rossby wave patterns present in Ψ_{bc}. The speeds detected from a Radon transform of the Hovmöller diagram of meridional velocity in OFES and the two-layer model are about -0.04 and $-0.042\,\mathrm{m\,s^{-1}}$, respectively. They are consistent with the typical value for a first-mode baroclinic Rossby wave at 26.5°N. The annual cycle of the GS is also seen in the anomalous thermocline changes along the western boundary in July and October (Figs. 6c,d). The thermocline anomalies along both boundaries are meridionally coherent within about 15°, a scale consistent with that detected in Fig. 2. Therefore, the dynamics evaluated at 26.5°N is representative for the northern subtropical region.

c. Comparison of Gulf Stream, Ekman, and midocean transports

In accordance to the in situ observations by the 26.5°N array, we split the MOC from the two-layer model into GS, EK, and UMO components and compare them to OFES (Fig. 4). Note that the two-layer model does not include the thermohaline circulation, so the annual-mean value of each component from OFES is added to the two-layer model result. As shown in Fig. 4, both the amplitude and phase for the seasonal-varying MOC in the two models agree very well. Because the same winds are used in both models, their Ekman transports exhibit exactly the same annual cycle. Peak GS transport

occurs in July in both models, while the seasonal minimum in the two-layer model occurs in October, a month earlier than the November minimum in OFES. This difference could be induced by neglected nonlinear advective effects in the two-layer model; also the simple stratification parameter in the two-layer model might not exactly capture the correct phase speed of the coastal baroclinic waves that are believed to play a role in the seasonal cycle of the GS (Anderson and Corry 1985). Nevertheless, the essential characteristics of the seasonal GS are well captured by the two-layer model, suggesting that the seasonal cycle of the GS in OFES is mainly driven by linear processes. This is consistent with the study of Anderson and Corry (1985), who also used a linear model and reproduced most of the observed GS seasonality. For the UMO, the two-layer model is able to produce the minimum in spring and maximum in fall. Although the two-layer model has a slightly lower minimum in spring, its overall cycle is consistent with OFES and the in situ observations.

d. Analogy with a simple, forced Rossby wave model

The dynamics underlying this UMO response can be further investigated using a simple, linear, forced Rossby wave model. On time scales longer than the inertial period, the oceanic response to wind stress curl forcing can be expressed by

$$\frac{\partial P_n}{\partial t} - \beta c_n^2 f^{-2} \frac{\partial P_n}{\partial x} = -c_n^2 f^{-1} F_n \nabla \times \tau,$$

where P_n is pressure for the nth vertical mode, t is time, x is the distance eastward, f is the Coriolis parameter, β is the planetary vorticity gradient, c_n is the nth mode long gravity wave speed, τ is wind stress, and F_n is the projection of the forcing onto vertical modes (Sturges et al. 1998):

$$F_n = \frac{1}{D_{\text{mix}}} \int_{-D_{\text{mix}}}^{0} \varphi_n(z)\, dz \Big/ \int_{-D}^{0} \varphi_n(z)^2 \, dz.$$

Here, D is water depth, D_{mix} is the surface mixed layer depth, and $\varphi_n(z)$ is the nth vertical mode eigenfunction, which is calculated from the OFES hydrographic data along 26.5°N. The variables φ_n and c_n are chosen from a representative longitude (60°W) for the calculation. Only the first baroclinic mode is used here, that is, $n = 1$. The equation is integrated from zero initial conditions using the climatological seasonal cycle of wind stress curl anomaly at 26.5°N extracted from the OFES 1980–2009 monthly fields. An equilibrium seasonal cycle of P_1 is reached after about 20 yr of integration.

The meridional geostrophic transport above h_{moc} can be calculated according to

$$T(x) = \int_{h_{\text{moc}}}^{0} v(x,z)\, dz = \int_{h_{\text{moc}}}^{0} \frac{1}{\rho f} \frac{\partial P_1}{\partial x} \varphi_1(z)\, dz,$$

and the streamfunction computed from $T(x)$ is shown in Fig. 11a. Its spatial pattern and phase are overall consistent with that in OFES and the two-layer model (Figs. 7b and 8b). Near the eastern boundary the seasonality is similar to that in the two-layer model and OFES, in terms of both phase and amplitude. This implies that the forced Rossby wave model captures the essential physics accounting for the upper-layer transport variations near the eastern boundary. However, the seasonal cycle at the western edge of the interior in the Rossby wave model has weaker amplitude than that in OFES and the two-layer model. The reason is that, unlike the two-layer model or OFES, the Rossby wave model cannot account for any wave reflection/interaction processes at the western boundary. Therefore, the zonally integrated meridional transport in the Rossby wave model is dependent on the particular phasing of the waves as they strike the Bahamas, and its seasonal cycle is sensitive to the wave speed and basin width. In the case shown (Fig. 11), the phasing of the wave arrivals at the western boundary leads to a relatively weak basinwide transport anomaly, but this could easily be much larger (or smaller) if the phase speed of the waves was slightly changed. The wave reflection in the OFES and the two-layer model largely reduces the effect of the waves impinging onto the western boundary, resulting in a seasonal cycle of UMO in the two-layer model that has similar phase and amplitude as that of the meridional transport near the eastern boundary in the Rossby wave model (Fig. 11b). This further confirms that the uplift (depression) of the thermocline forced by the wind stress curl in the east has a dominant effect on the seasonality of UMO.

e. Sensitivity to wind forcing

Chidichimo et al. (2010) and Kanzow et al. (2010) found that the observed seasonal cycle of interior flow has a 6.7-Sv peak-to-peak amplitude, and the pressure (density) anomalies at the eastern boundary leads to a seasonal cycle of 5.2 Sv. With the same type of Rossby wave model used here, Kanzow et al. (2010) successfully reproduced a seasonal cycle with comparable amplitude and phase to the observations. The seasonal cycle obtained by our study, however, has a much weaker amplitude than that in Kanzow et al. (2010). The main reason for the different amplitudes in our study and theirs is that different wind fields are used. Kanzow et al. (2010) used wind stresses derived from the Scatterometer Climatology of Ocean Winds (SCOW) that correctly
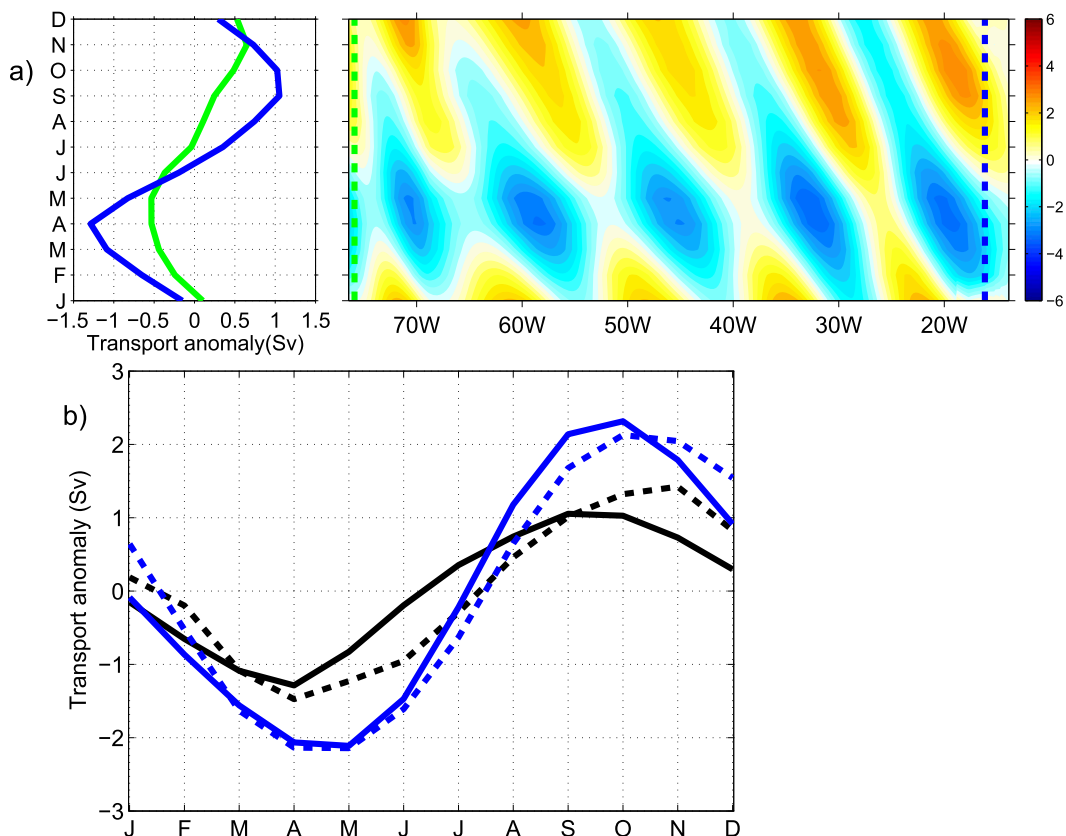
FIG. 11. (a) Streamfunction for the baroclinic geostrophic flow simulated by the Rossby wave model at 26.5°N is shown in the right (Sv). The seasonal cycle near the eastern (blue) and western (green) boundary are shown at the left, and their locations are marked by blue and green dashed lines, respectively. The selected locations near the eastern and western boundary are the same as those in the two-layer model (see text). (b) Seasonal cycle of the UMO from the two-layer model forced by NCEP–NCAR winds (black dashed line) and from the two-layer model forced by SCOW winds (blue dashed line). The seasonality of eastern boundary from the Rossby wave model forced by NCEP–NCAR winds and SCOW winds are shown by the black and blue solid lines, respectively. The comparison between two-layer model and Rossby wave model results illustrates that the seasonal cycle in the two-layer model is mostly contributed by the eastern boundary.

preserves the WSC near the land/ocean boundaries (Risien and Chelton 2008), whereas both OFES and the two-layer model use the NCEP–NCAR wind field. The SCOW winds have a seasonal WSC variation at the eastern boundary that is about 2–3 times stronger than that in NCEP–NCAR. This causes a much larger local response of the density field at the eastern boundary and a much larger seasonal AMOC variation. To verify this, the SCOW winds are also used to force the linear Rossby wave model and the two-layer model, and their corresponding seasonal cycles are shown for comparison in Fig. 11b. In contrast to the NCEP–NCAR dataset, the SCOW winds produce a seasonal cycle with more comparable amplitude to the observed AMOC seasonal variability in both the Rossby wave model and two-layer model. Nearly all of this difference is due to the differences in the SCOW and NCEP–NCAR winds near the eastern boundary.

Therefore, the weaker boundary wind stress curl in the NCEP–NCAR dataset is the main reason that OFES as well as the two-layer model underestimate the observed MOC seasonal variability at 26.5°N (Fig. 4).

5. AMOC seasonal cycle at 6°N

We selected 6°N to study the seasonal variations in the tropical Atlantic Ocean where both the Ekman and geostrophic transport have large seasonal fluctuations. As shown in Fig. 2, the Ekman transport has a seasonal cycle of 14-Sv peak-to-peak amplitude with a maximum in January and minimum in August. The annual peak-to-peak amplitude for the geostrophic transport is 9 Sv, and its minimum is in May and its maximum is in October. Similar seasonality can be found in the two-layer model results, suggesting that the variations in both
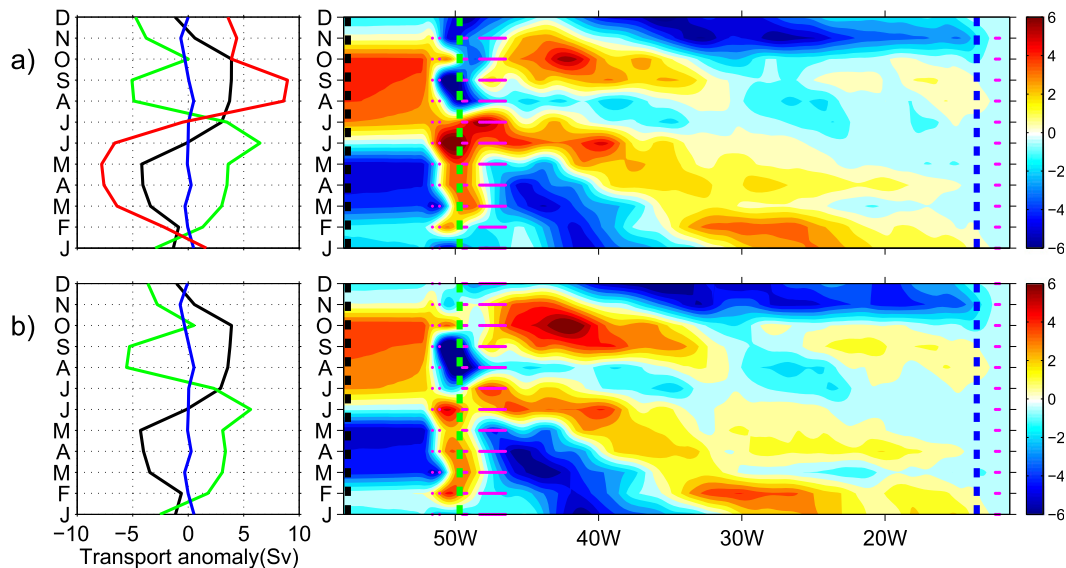
FIG. 12. As in Figs. 7a,b but for (a) upper-layer meridional geostrophic streamfunction (Ψ_1) and (b) baroclinic streamfunction (Ψ_{bc}) from the OFES model (1980–2009) at 6°N. The dashed lines mark the locations for the offshore edge of the eastern boundary layer (blue), western point of the interior ocean (green), and the western basin boundary (black). The seasonal cycle at the three points in each streamfunction are also shown at left in their corresponding colors. Red line denotes the NBC (Sv).

Ekman and geostrophic transport at 6°N are largely controlled by the wind forcing. In fact, the seasonal wind stress forcing in this region is controlled mainly by the annual migration of the ITCZ, which not only changes the zonal wind stress but also modifies the wind stress curl across the basin interior. The variable wind stress curl modifies the interior flows that feed the western boundary current, the North Brazil Current (NBC) (Johns et al. 1998). Similar to 26.5°N, the seasonal cycle near the eastern basin boundary, western point of the interior ocean, and western basin boundary are selected in both the OFES and two-layer model. A point twice the Rossby deformation radius away from the eastern basin boundary is selected as the eastern point, while the location of the maximum (minimum) of the interior streamfunction anomaly is chosen as the western point of the interior ocean. The latter choice corresponds roughly to the outer edge of the western boundary current in each simulation, because, unlike 26.5°N, there is no geographic feature (i.e., the Bahamas) that clearly separates the interior domain from the western boundary domain.

a. Seasonal variability of the upper-layer streamfunction

Figure 12 displays the seasonal anomaly of Ψ_1 in OFES. Near the eastern boundary there is no significant seasonal variability (blue line) because the wind stress curl near the eastern boundary is relatively weak (Fig. 13c).

(Notably, the wind stress curl shown here is very similar to the SCOW data.) From the eastern boundary to 30°W, Ψ_1 has a maximum in February and a minimum in November, while from 30° to 45°W the seasonal cycle is modified and has semiannual variation. From 45° to 50°W, the seasonal fluctuations are further changed by the retroflection of the NBC and give rise to an annual cycle maximum in June and minimum in September. The NBC retroflection also induces large interannual variations so that the seasonal cycles near 48°W are not robust. The main part of the NBC is located between 50° and 52°W, and at its inshore edge (at ~52°W), the seasonal variability of the meridional transport quickly and completely shifts to a cycle with a minimum in April and maximum in October, which remains nearly constant from there to the western boundary. This implies that the NBC plays a fundamental role in shaping the seasonal cycle of the cumulative geostrophic transport across the basin at 6°N.

In the two-layer model (Fig. 13), a very similar annual cycle occurs for the cumulative geostrophic transport across the full section, but there are significant differences in the interior. East of 45°W, the two-layer model does not reproduce the seasonal variations in OFES. This is because the local meridional transport in OFES is strongly affected by the nonlinear retroflection of the NBC and the large-scale interior meandering pattern of the North Equatorial Current, which is not represented in the linear two-layer model (e.g., Fig. 6). However, the
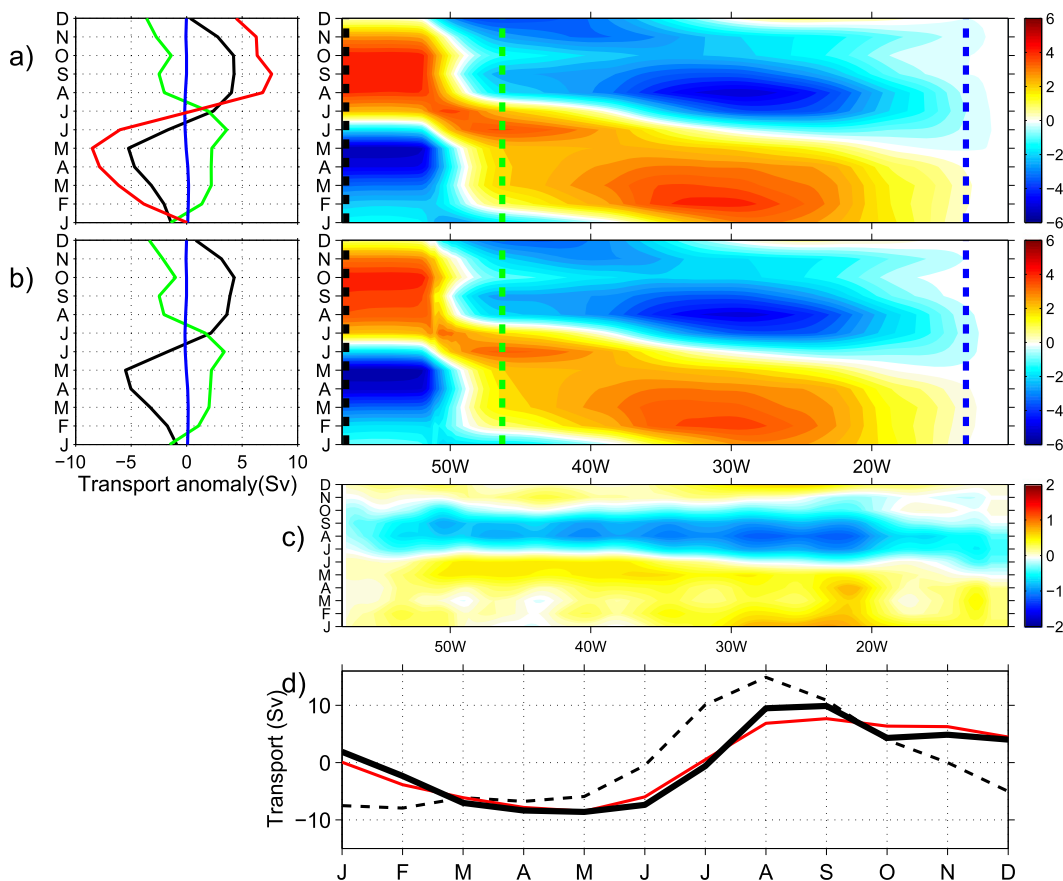
FIG. 13. (a),(b) As in Fig. 12, but for the two-layer model. (c) Wind stress curl calculated from the wind forcing used in the two-layer model at 6°N (10^{-7} N m^{-3}). (d) Seasonal anomaly of the NBC in OFES (thick solid) and two-layer model (red). Dashed line is the boundary current transport derived from the stationary Sverdrup balance.

seasonal cycle for the cumulative interior flow (green line in Figs. 12a and 13a) is consistent in both models, and westward of this point they remain very similar, leading to a nearly identical seasonal variability in the zonally integrated flow (black lines in Figs. 12a and 13a). As shown in Figs. 12b and 13b, Ψ_{bc} has similar spatial structure and temporal variations to that of the upper-layer geostrophic transport (Ψ_1). The term Ψ_{bt} has much weaker variability (not shown), indicating again that the seasonal fluctuations of the upper-geostrophic transport are mostly controlled by baroclinic processes.

b. Role of the North Brazil Current

The seasonal variability in both Ψ_1 and Ψ_{bc} is a well-known feature of the tropics and is a consequence of the rapid adjustment of the tropical ocean by baroclinic planetary waves (Philander and Pacanowski 1980). The interior geostrophic flow is forced by the WSC associated with the ITCZ migration. It takes several months for the changes in the interior ocean to be communicated into the WBC. In February (July) anomalous

northward (southward) interior geostrophic flow occurs east of 30°W (Figs. 13a,b), but the NBC does not reach its corresponding seasonal maximum (minimum) until May (September) (red line in Figs. 12a and 13a). The seasonally changing circulation patterns associated with this are shown in Fig. 6, where 6°N lies near the boundary between the oscillating basin-scale patterns to the north and south. A maximum cyclonic (anticyclonic) circulation anomaly occurs to the north of 6°N during boreal spring (fall), with opposite circulation anomalies to the south, which correspond to the spinup and spin-down of the tropical and equatorial upper-ocean gyres through the action of the baroclinic planetary waves. Figure 13d shows the NBC transport cycle in OFES, two-layer model, and that calculated from a stationary Sverdrup balance. The NBC in OFES has its minimum in spring and maximum in fall, a cycle very similar to that of the basinwide upper-geostrophic transport. Because of the lack of a thermohaline component in the two-layer model, it does not reproduce the mean NBC transport, but the essential features of the seasonal cycle
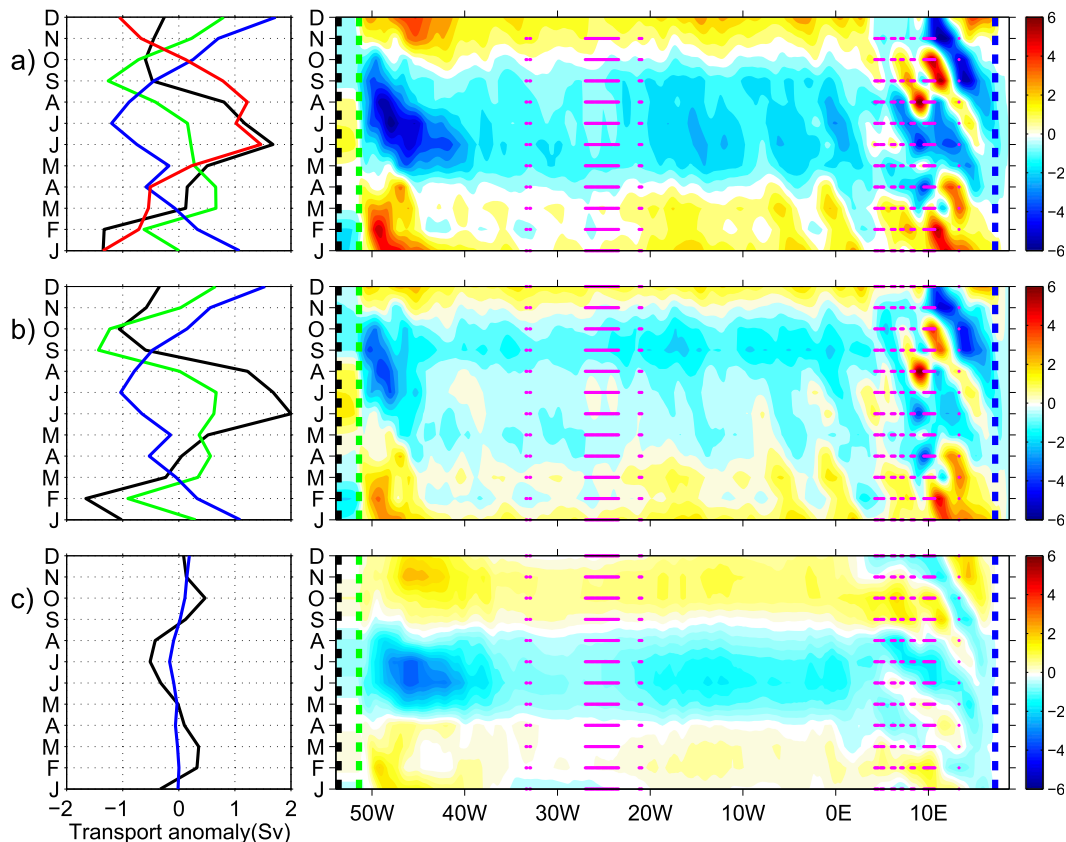
FIG. 14. As in Fig. 7, but for 34.5°S. The red line in (a) is the seasonal cycle of the BC, taken as the difference of the streamfunction at basin boundary (black dashed line) and western interior point (the continental shelf where water depth is h_{moc}; green dashed line).

are well captured by the linear wind-driven two-layer model. The difference between the NBC in the Sverdrup cycle and two-layer model reflects the delayed response to the remote wind stress curl due to the propagation of the baroclinic waves. Particularly, the spring minimum is absent in the Sverdrup cycle. The lag of the NBC with respect to the interior leads to an "excess" NBC transport in fall and a corresponding "deficit" in spring that determines the overall seasonal cycle of the upper-geostrophic transport. Therefore, the AMOC seasonal cycle at 6°N is in fact mainly a consequence of the lagged adjustment of the NBC to the interior WSC forcing. This incomplete compensation between the boundary current and interior ocean due to the oceanic adjustment is the dominating mechanism for the geostrophic part of the AMOC throughout the tropics.

6. Seasonal AMOC cycle at 34.5°S

We selected 34.5°S to study the seasonal variability in the southern subtropical ocean. At this latitude the Ekman transport has a minimum in February and

maximum in June with a peak-to-peak amplitude of 6 Sv, and the geostrophic transport has its minimum in January and maximum in June with a peak-to-peak amplitude of 2.5 Sv (Fig. 2). The nearly out of phase Ekman and geostrophic transports, and larger amplitude in Ekman transport, leads to the dominance of Ekman transport in shaping the seasonal AMOC at 34.5°S.

As shown in Fig. 14a, the seasonal anomaly of Ψ_1 in OFES shows an annual cycle of ±1.5-Sv amplitude at the edge of the eastern boundary (blue line), which is twice the Rossby deformation radius away from the eastern boundary. Between 5° and 15°E, larger fluctuations are associated with Agulhas rings passing northward across the section. These rings not only modify the local meridional flow but also generate substantial interannual variations, so that the derived annual cycle here is not robust. West of 0°, the impact of the Agulhas ring is not obvious and the seasonal cycle of Ψ_1 presents a structure that is very similar to that at the edge of the eastern boundary zone, and this remains stable across most of the interior basin. Westward of 40°W, this signal becomes significantly amplified by additional meridional
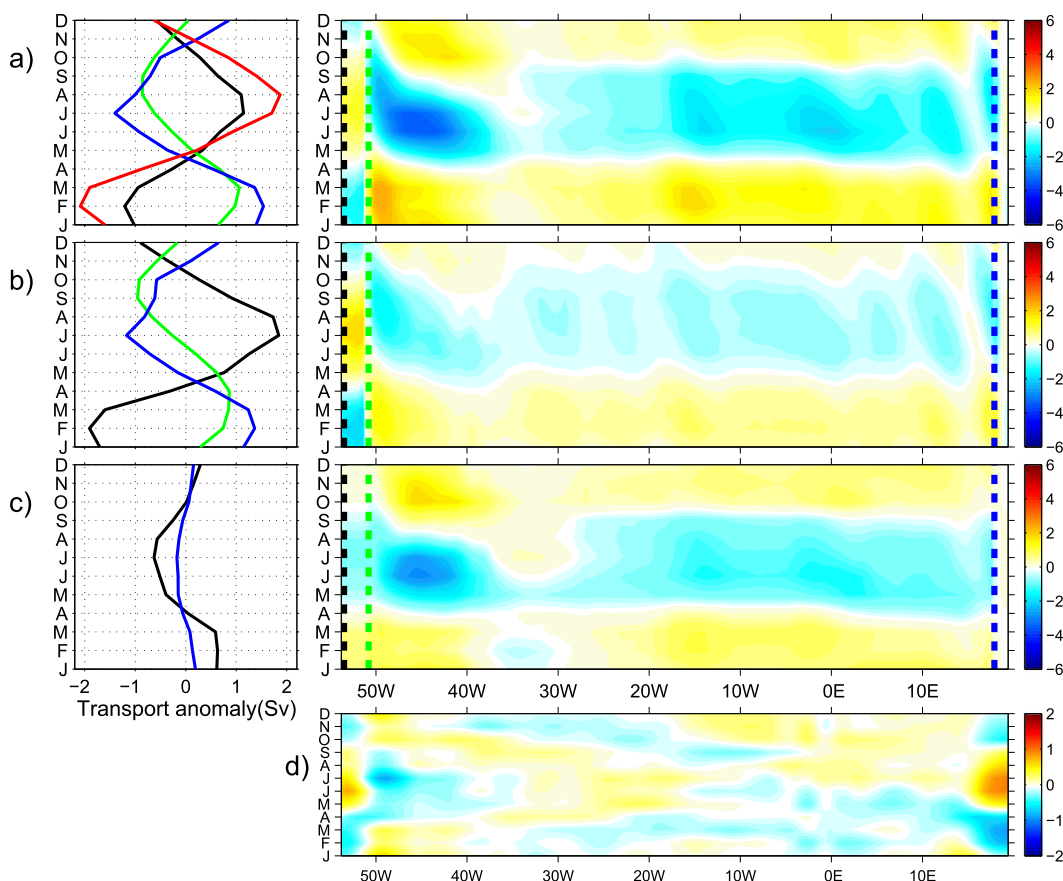
FIG. 15. (a)–(c) As in Fig. 14, but for the two-layer model at 34.5°S. (d) Wind stress curl calculated from the wind forcing used in the two-layer model at 34.5°S (10^{-7} N m^{-3}).

flow in the western part of the basin. At the continental shelf where the water depth is h_{moc} (green dashed line), Ψ_1 features a minimum in September and maximum in March. Including the WBC [the Brazil Current (BC)], however (red line in Fig. 14a), the annual cycle is fundamentally changed and leads to a cycle with a minimum in February and maximum in June when integrated across the full section.

A similar seasonal cycle of the meridional geostrophic transport is simulated by the two-layer model (Fig. 15). Near the eastern boundary, the seasonal cycle in the two-layer model generally agrees with that in the OFES, although its maximum occurs in February rather than December. The Agulhas rings near the eastern boundary are not reproduced by the two-layer model, but they do not affect the seasonal cycle of the zonally integrated transport west of 0°. What is captured by both OFES and the two-layer model is the relatively uniform seasonal variability in the interior ocean and the rapid shift across the BC to a phase that is almost opposite that in the interior ocean (Figs. 14a and 15a). It is interesting to note also that the interior modulations of Ψ_1 by the annual

baroclinic Rossby waves are much less pronounced in both OFES and the two-layer model at 34.5°S than at 26.5°N. This is due to the different structure of the WSC across the basin. As shown in Fig. 8d, the annual cycle of the WSC at 26.5°N has a broad coherent pattern across the whole basin so that the Rossby waves generated at the eastern boundary are simply modulated by the annual forcing as they propagate westward and maintain their energy. However, the WSC at 34.5°S has a weak seasonal cycle and varying phase across the basin (Fig. 15d), such that the local forcing tends to damp the propagating Rossby waves and reduces their amplitudes in the central part of the basin. The same type of behavior occurs in the simple forced Rossby wave model for the South Atlantic (not shown).

A separation of the geostrophic current into barotropic (Ψ_{bt}) and baroclinic (Ψ_{bc}) components indicates that Ψ_1 is controlled by both barotropic and baroclinic processes. Near the eastern boundary, the seasonal fluctuations in Ψ_{bc} are very similar to that in Ψ_1 (blue lines in Figs. 14a and 15a). This suggests that it is the uplift and depression of the thermocline that controls

the eastern boundary changes, dynamics similar to that at 26.5°N. The vertical motions of the thermocline are forced by the wind stress curl near the eastern boundary (Fig. 15d). As shown in Fig. 6, the interface anomaly along the eastern boundary is coherent between 25° and 35°S, indicating that the seasonal cycle shown here is regionally forced over about 10° meridional extent. Note that the wind stress curl anomaly in SCOW has similar phase and amplitude to that in NCEP–NCAR (not shown).

In the interior ocean, Ψ_{bc} is affected by the westward-propagating Rossby waves, analogous to that at 26.5°N, but as noted above with lesser amplitude. The contribution of the barotropic streamfunction Ψ_{bt} to the upper-layer streamfunction Ψ_1 is relatively greater at 34.5°S than at 26.5°N, so that Ψ_1 reflects attributes of both Ψ_{bt} and Ψ_{bc}. The seasonally varying barotropic circulation is more complicated than in the Northern Hemisphere and shows two gyre-scale patterns (Figs. 10c,d). South of 30°S, the anomalous ocean circulation is dominated by an anticlockwise (clockwise) gyre in February (July), while north of 30°S a clockwise (anticlockwise) gyre is evident in February (July). These two different barotropic gyre structures are generated by opposite seasonal cycles of the wind stress curl south and north of 35°S (not shown).

Similar to the results at 26.5°N, however, the net impact of the barotropic circulation on the seasonal AMOC variability is small. At the continental shelf (green dashed line in Figs. 14 and 15), the barotropic circulation is largely compensated so that Ψ_{bc} dominates the annual cycle in Ψ_1 when zonally integrated across the basin (black line in Figs. 14c and 15c). Especially the rapid transition of the annual cycle at the edge of the continental shelf is mostly included in Ψ_{bc}, demonstrating that it is the shallow part of the BC in depths $\leq 1000\,\mathrm{m}$ that controls the seasonal AMOC cycle. As shown in Fig. 6, the seasonal anomalies of the BC transport have a meridional scale of about 15°, or perhaps greater (Figs. 6a,c), and are probably associated with both local and remote coastal wind forcing that cause an uplift of the coastal thermocline in austral winter and a depression of the coastal thermocline in austral summer. Part of the BC annual cycle is also modulated by the Rossby wave pattern that produces more localized, and opposite signed, thermocline depth anomalies just offshore of the western boundary layer. This process is different from 26.5°N because of the blocking effect of the Bahamian Islands.

We note that the barotropic circulation also contributes to the total seasonal changes of the BC. As shown in Figs. 10c and 10d, the intensified barotropic streamlines near the western boundary indicate that the southward BC becomes stronger in February (July) and weaker in

July (February) for the regions south (north) of 30°S. This is consistent with the seasonal changes of the BC at 34.5°S in both OFES and the two-layer model (red line in Figs. 14a and 15a), implying that the seasonal spinup (spindown) of the barotropic circulation leads to acceleration (deceleration) of the BC as indicated above. However, the seasonality of the BC induced by the barotropic circulation is mostly compensated and does not significantly contribute to the geostrophic transport across the basin.

7. Discussion and summary

The seasonal cycle of the AMOC simulated by an eddy-resolving ocean model is investigated in this study. The seasonal variability is largest in the northern tropical Atlantic region where the peak-to-peak amplitude is 10 Sv, with a maximum in boreal winter and minimum in boreal autumn. The variations in subtropical regions are smaller with peak-to-peak amplitudes of 4–6 Sv and varying phases. By splitting the AMOC variability into Ekman and geostrophic transport components, the contribution of each to the total AMOC variability can be examined. It is found that both contributions are characterized by substantial variations throughout the year. Their seasonal cycles are almost out of phase in the tropical Atlantic region, and the Ekman transport has larger amplitude, so that the seasonality of the AMOC is dominated by the Ekman component. In subtropical regions, however, their magnitudes are comparable and their phases vary with location so that both of them determine the seasonal cycle of the AMOC. The mechanisms governing the geostrophic component depend on how the barotropic and baroclinic circulation modes develop across the basin on seasonal time scales.

To explore the dynamics responsible for the seasonal cycle of AMOC and its components, a linear two-layer model forced by climatological NCEP–NCAR winds is utilized. The similarity of the AMOC seasonal cycle between the two-layer model and OFES, which is forced both by wind and buoyancy fluxes, indicates that the variability of the AMOC on seasonal time scales is mainly associated with the wind forcing and that the two-layer model includes the fundamental dynamics to reproduce this variability. It is shown that the depth-dependent geostrophic transport is modulated by the oceanic adjustment to wind forcing, in which coastal boundary currents, baroclinic Rossby waves in the ocean interior, and large-scale barotropic flow adjustment play a vital role.

To identify the dominating mechanism in different regions, three latitudes, 26.5°N, 6°N, and 34.5°S, are selected to represent the northern subtropical, equatorial, and southern subtropical ocean. At each latitude, the

zonally accumulated streamfunction of the meridional geostrophic flow above h_{moc} indicates that the geostrophic seasonal cycle is shaped either by the WBC or determined by both the WBC and interior transports. Based on thermal wind theory, the interior flow in the deep ocean is determined by the density difference across the basin. The factors affecting the interior transport are the anomalies carried by westward-propagating Rossby waves toward the western boundary and the fluctuations forced by the local wind stress curl. These physics are incorporated into a linear Rossby wave model that successfully accounts for the seasonal cycle of the upper-midocean transport at 26.5°N.

One important result in this study is the role of the western boundary current (WBC) in determining the basinwide geostrophic transport and AMOC seasonal cycle. In the tropical region, the WBC is controlled by the time-dependent Sverdrup balance established by tropical baroclinic Rossby waves. The lagged response of the WBC to the interior wind forcing causes a seasonal imbalance of the net upper-layer flow across the basin, which determines the annual cycle of the AMOC. On the other hand, in the extratropics the seasonal cycle of the WBC is not dominantly controlled by the planetary waves; instead it is determined mostly by local and remote forcing communicated along the western boundary. Local and remote wind forcing along the eastern boundary can also contribute significantly to the seasonal AMOC cycle, which, for example, is found to be the dominant mechanism at 26.5°N.

The geostrophic transport across the basin is ultimately determined by the pressure difference between the basin boundaries. In a simplified two-layer ocean, like the simple model used in this study, the seasonal changes in the zonally integrated baroclinic streamfunction Ψ_{bc}, which dominates the seasonal AMOC variation at all latitudes, is related to the change in interface depth on the boundaries. The relative importance of each boundary, at any given latitude, can be evaluated by the ratio of their annual amplitude. Figure 16 displays the latitudinal distribution of this ratio estimated from the two-layer model, together with the annual amplitudes of basinwide geostrophic transport. North of 10°N, the ratio is larger than one, indicating that the eastern boundary has a larger contribution to the seasonal AMOC cycle. In the equatorial region, however, the ratio is much less than one, pointing out the dominant role of the western boundary. In the southern subtropical region, both boundaries tend to have comparable contributions, reflected by ratios that range from 0.5 to 1.5. The meridional distance over which these coastal forcing regions are coherent are typically about 10°–15° along either boundary, and these
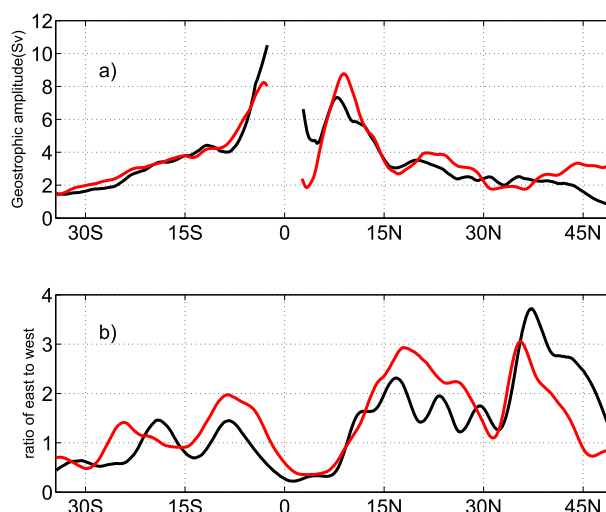

FIG. 16. (a) Latitudinal distribution of the annual amplitude of the basinwide geostrophic AMOC from the two-layer model forced by NCEP–NCAR (black) and SCOW (red); (b) ratio of the annual amplitude of the interface anomaly at the eastern to western boundary. Results from the two-layer model forced by NCEP–NCAR and SCOW are shown in black and red, respectively. The annual amplitude at each latitude represents the difference between the max and min values of the annual cycle.

are roughly the same scales over which the AMOC seasonal variation is meridionally coherent.

The dynamical processes evaluated in this study point out the important factors to correctly simulate the seasonal cycle of MOC, and this might shed light on model-based MOC hindcast studies. As noted previously, the wind stress curl at the boundaries in NCEP–NCAR appears to be unrealistically low, at least at 26.5°N. To assess the sensitivity of the meridional geostrophic transport to different wind forcing, we ran the two-layer model using the SCOW dataset, which is designed to better preserve wind stress patterns near the ocean boundaries. In the Southern Hemisphere the geostrophic AMOC amplitudes are generally similar to those forced by the NCEP–NCAR dataset, and they are generally larger than the NCEP–NCAR run in the Northern Hemisphere (Fig. 16). The ratio of eastern to western boundary contributions to the basinwide geostrophic MOC seasonal cycles is also somewhat different in the NCEP–NCAR and SCOW runs. Therefore, deficiencies in the wind forcing near the basin boundaries, such as appear to occur in the NCEP–NCAR reanalysis winds used to drive the OFES model, can lead to inaccuracies in the simulation of the magnitude of the AMOC seasonal cycle.

The overall results of this study point to the dominant role of eastern and western boundary currents in the extratropics in determining the basinwide geostrophic AMOC seasonal cycle. While both baroclinic planetary

waves and barotropic gyres set up by the interior WSC forcing strongly affect the total upper-layer geostrophic circulation at any location, they do not contribute significantly to the seasonal AMOC cycle because of internal compensation when integrated over the full width of the basin. We find further that the eastern boundary contribution to the AMOC cycle is generally dominant in the Northern Hemisphere, while this is not true in the Southern Hemisphere. The dominance of the eastern boundary contribution that has been demonstrated by the 26.5°N array is therefore not a result that holds over the whole basin. The seasonal AMOC variability in the tropics is fundamentally different in that the interior upper-ocean geostrophic flow driven by the basinwide Sverdrup forcing is an integral part of the response. Its lagged compensation by the WBC, set by the relatively fast adjustment time scale of tropical baroclinic Rossby waves, determines the basinwide geostrophic AMOC seasonal cycle in the tropics. Here the eastern boundary plays a much more limited role, and it is primarily the WBC response to the interior wind forcing, rather than local or regional forcing effects near the boundaries, that dominates the geostrophic contribution to the AMOC seasonal cycle.

REFERENCES

Anderson, D. L. T., and A. E. Gill, 1975: Spin-up of a stratified ocean, with applications to upwelling. *Deep-Sea Res.,* **22,** 583–596, doi:10.1016/0011-7471(75)90046-7.

——, and P. D. Killworth, 1977: Spin-up of a stratified ocean, with topography. *Deep-Sea Res.,* **24,** 709–732, doi:10.1016/0146-6291(77)90495-7.

——, and R. A. Corry, 1985: Seasonal transport variations in the Florida Straits: A model study. *J. Phys. Oceanogr.,* **15,** 773–786, doi:10.1175/1520-0485(1985)015<0773:STVITF>2.0.CO;2.

——, K. Bryan, A. E. Gill, and R. C. Pacanowski, 1979: The transient response of the North Atlantic: Some model studies. *J. Geophys. Res.,* **84,** 4795–4815, doi:10.1029/JC084iC08p04795.

Atkinson, C. P., H. L. Bryden, J. J.-M. Hirschi, and T. Kanzow, 2010: On the seasonal cycles and variability of Florida Straits, Ekman and Sverdrup transports at 26°N in the Atlantic Ocean. *Ocean Sci.,* **6,** 837–859, doi:10.5194/os-6-837-2010.

Baehr, J., J. Hirschi, J. O. Beismann, and J. Marotzke, 2004: Monitoring the meridional overturning circulation in the North Atlantic: A model-based array design study. *J. Mar. Res.,* **62,** 283–312, doi:10.1357/0022240041446191.

Biastoch, A., C. W. Böning, J. Getzlaff, J.-M. Molines, and G. Madec, 2008: Causes of interannual–decadal variability in the meridional overturning circulation of the midlatitude North Atlantic Ocean. *J. Climate,* **21,** 6599–6615, doi:10.1175/2008JCLI2404.1.

Bingham, R. J., C. W. Hughes, V. Roussenov, and R. G. Williams, 2007: Meridional coherence of the North Atlantic meridional overturning circulation. *Geophys. Res. Lett.,* **34,** L23606, doi:10.1029/2007GL031731.

Böning, C. W., and P. Herrmann, 1994: Annual cycle of poleward heat transport in the ocean: Results from high-resolution modeling of the North and equatorial Atlantic. *J. Phys. Oceanogr.,* **24,** 91–107, doi:10.1175/1520-0485(1994)024<0091:ACOPHT>2.0.CO;2.

Bryan, K., 1982: Seasonal variation in meridional overturning and poleward heat transport in the Atlantic and Pacific Oceans: A model study. *J. Mar. Res.,* **40,** 39–53.

Chidichimo, M. P., T. Kanzow, S. A. Cunningham, W. E. Johns, and J. Marotzke, 2010: The contribution of eastern-boundary density variations to the Atlantic meridional overturning circulation at 26.5°N. *Ocean Sci.,* **6,** 475–490, doi:10.5194/os-6-475-2010.

Cunningham, S. A., and Coauthors, 2007: Temporal variability of the Atlantic meridional overturning circulation at 26.5°N. *Science,* **317,** 935–938, doi:10.1126/science.1141304.

Czeschel, L., C. Eden, and R. J. Greatbatch, 2012: On the driving mechanism of the annual cycle of the Florida Current transport. *J. Phys. Oceanogr.,* **42,** 824–839, doi:10.1175/JPO-D-11-0109.1.

Delworth, T. L., S. Manabe, and R. J. Stouffer, 1993: Interdecadal variations of the thermohaline circulation in a coupled ocean–atmosphere model. *J. Climate,* **6,** 1993–2011, doi:10.1175/1520-0442(1993)006<1993:IVOTTC>2.0.CO;2.

Dong, S., S. Garzoli, M. Baringer, C. Meinen, and G. Goni, 2009: Interannual variations in the Atlantic meridional overturning circulation and its relationship with the net northward heat transport in the South Atlantic. *Geophys. Res. Lett.,* **36,** L20606, doi:10.1029/2009GL039356.

Garzoli, S., and M. O. Baringer, 2007: Meridional heat transport determined with expandable bathythermographs—Part II: South Atlantic transport. *Deep-Sea Res. I,* **54,** 1402–1420, doi:10.1016/j.dsr.2007.04.013.

Hirschi, J., and J. Marotzke, 2007: Reconstructing the meridional overturning circulation from boundary densities and the zonal wind stress. *J. Phys. Oceanogr.,* **37,** 743–763, doi:10.1175/JPO3019.1.

——, P. D. Killworth, and J. R. Blundell, 2007: Subannual, seasonal, and interannual variability of the North Atlantic meridional overturning circulation. *J. Phys. Oceanogr.,* **37,** 1246–1265, doi:10.1175/JPO3049.1.

Jayne, S. R., and J. Marotzke, 2001: The dynamics of ocean heat transport variability. *Rev. Geophys.,* **39,** 385–411, doi:10.1029/2000RG000084.

Johns, W. E., T. N. Lee, R. C. Beardsley, J. Candela, R. Limeburner, and B. Castro, 1998: Annual cycle and variability of the North

Brazil Current. *J. Phys. Oceanogr.,* **28,** 103–128, doi:10.1175/1520-0485(1998)028<0103:ACAVOT>2.0.CO;2.

——, L. M. Beal, M. O. Baringer, J. R. Molina, S. A. Cunningham, T. Kanzow, and D. Rayner, 2008: Variability of shallow and deep western boundary currents off the Bahamas during 2004–05: Results from the 26°N RAPID–MOC array. *J. Phys. Oceanogr.,* **38,** 605–623, doi:10.1175/2007JPO3791.1.

——, and Coauthors, 2011: Continuous, array-based estimates of Atlantic Ocean heat transport at 26.5°N. *J. Climate,* **24,** 2429–2449, doi:10.1175/2010JCLI3997.1.

Kalnay, E., and Coauthors, 1996: The NCEP/NCAR 40-Year Reanalysis Project. *Bull. Amer. Meteor. Soc.,* **77,** 437–471, doi:10.1175/1520-0477(1996)077<0437:TNYRP>2.0.CO;2.

Kanzow, T., and Coauthors, 2007: Observed flow compensation associated with the MOC at 26.5°N in the Atlantic. *Science,* **317,** 938–941, doi:10.1126/science.1141293.

——, H. L. Johnson, D. P. Marshall, S. A. Cunningham, J. J.-M. Hirschi, A. Mujahid, H. L. Bryden, and W. E. Johns, 2009: Basinwide integrated volume transports in an eddy-filled ocean. *J. Phys. Oceanogr.,* **39,** 3091–3110, doi:10.1175/2009JPO4185.1.

——, and Coauthors, 2010: Seasonal variability of the Atlantic meridional overturning circulation at 26.5°N. *J. Climate,* **23,** 5678–5698, doi:10.1175/2010JCLI3389.1.

Knight, J. R., R. J. Allan, C. K. Folland, M. Vellinga, and M. E. Mann, 2005: A signature of persistent natural thermohaline circulation cycles in observed climate. *Geophys. Res. Lett.,* **32,** L20708, doi:10.1029/2005GL024233.

Köhl, A., 2005: Anomalies of meridional overturning: Mechanisms in the North Atlantic. *J. Phys. Oceanogr.,* **35,** 1455–1472, doi:10.1175/JPO2767.1.

——, and D. Stammer, 2008: Variability of the meridional overturning in the North Atlantic from the 50-year GECCO state estimation. *J. Phys. Oceanogr.,* **38,** 1913–1930, doi:10.1175/2008JPO3775.1.

Lee, T. N., W. E. Johns, R. J. Zantopp, and E. R. Fillenbaum, 1996: Moored observations of western boundary current variability and thermohaline circulation at 26.5° in the subtropical North Atlantic. *J. Phys. Oceanogr.,* **26,** 962–983, doi:10.1175/1520-0485(1996)026<0962:MOOWBC>2.0.CO;2.

Longuet-Higgins, M. S., 1964: Planetary waves on a rotating sphere. *Proc. Roy. Soc. London,* **A279,** 446–473, doi:10.1098/rspa.1964.0116.

Lumpkin, R., and K. Speer, 2007: Global ocean meridional overturning. *J. Phys. Oceanogr.,* **37,** 2550–2562, doi:10.1175/JPO3130.1.

Masumoto, Y., 2010: Sharing the results of a high-resolution ocean general circulation model under a multi-discipline framework—A review of OFES activities. *Ocean Dyn.,* **60,** 633–652, doi:10.1007/s10236-010-0297-z.

——, and Coauthors, 2004: A fifty-year eddy-resolving simulation of the world ocean—Preliminary outcomes of OFES (OGCM for the Earth Simulator). *J. Earth Simul.,* **1,** 35–56.

McCarthy, G., and Coauthors, 2012: Observed interannual variability of the Atlantic meridional overturning circulation at 26.5°N. *Geophys. Res. Lett.,* **39,** L19609, doi:10.1029/2012GL052933.

Pedlosky, J., 1987: *Geophysical Fluid Dynamics.* Springer, 710 pp.

Philander, S. G. H., and R. C. Pacanowski, 1980: The generation of equatorial currents. *J. Geophys. Res.,* **85,** 1123–1136, doi:10.1029/JC085iC02p01123.

Rayner, D., and Coauthors, 2011: Monitoring the Atlantic meridional overturning circulation. *Deep-Sea Res. II,* **58,** 1744–1753, doi:10.1016/j.dsr2.2010.10.056.

Risien, C. M., and D. B. Chelton, 2008: A global climatology of surface wind and wind stress fields from eight years of QuikSCAT scatterometer data. *J. Phys. Oceanogr.,* **38,** 2379–2413, doi:10.1175/2008JPO3881.1.

Sasaki, H., M. Nonaka, Y. Masumoto, Y. Sasai, H. Uehara, and H. Sakuma, 2008: An eddy-resolving hindcast simulation of the quasiglobal ocean from 1950 to 2003 on the Earth Simulator. *High Resolution Numerical Modelling of the Atmosphere and Ocean,* K. Hamilton and W. Ohfuchi, Eds., Springer, 157–185, doi:10.1007/978-0-387-49791-4_10.

Sturges, W., B. G. Hong, and A. J. Clarke, 1998: Decadal wind forcing of the North Atlantic subtropical gyre. *J. Phys. Oceanogr.,* **28,** 659–668, doi:10.1175/1520-0485(1998)028<0659:DWFOTN>2.0.CO;2.

Talley, L. D., J. L. Reid, and P. E. Robbins, 2003: Data-based meridional overturning streamfunctions for the global ocean. *J. Climate,* **16,** 3213–3226, doi:10.1175/1520-0442(2003)016<3213:DMOSFT>2.0.CO;2.

Vellinga, M., and R. A. Woods, 2002: Global impacts of a collapse of the Atlantic thermohaline circulation. *Climatic Change,* **54,** 251–267, doi:10.1023/A:1016168827653.

Willis, J. K., 2010: Can in situ floats and satellite altimeters detect long-term changes in Atlantic Ocean overturning? *Geophys. Res. Lett.,* **37,** L06602, doi:10.1029/2010GL042372.

Zhang, L., and C. Wang, 2013: Multidecadal North Atlantic sea surface temperature and Atlantic meridional overturning circulation variability in CMIP5 historical simulations. *J. Geophys. Res.,* **118,** 5772–5791, doi:10.1002/jgrc.20390.

——, ——, and S.-K. Lee, 2014: Potential role of Atlantic warm pool-induced freshwater forcing in the Atlantic meridional overturning circulation: Ocean–sea ice model simulations. *Climate Dyn.*, doi:10.1007/s00382-013-2034-z.